INFORMATION TO USERS

This manuscript has been reproduced from the microfilm master. UMI films the text directly from the original or copy submitted. Thus, some thesis and dissertation copies are in typewriter face, while others may be from any type of computer printer.

The quality of this reproduction is dependent upon the quality of the copy submitted. Broken or indistinct print, colored or poor quality illustrations and photographs, print bleedthrough, substandard margins, and improper alignment can adversely affect reproduction.

In the unlikely event that the author did not send UMI a complete manuscript and there are missing pages, these will be noted. Also, if unauthorized copyright material had to be removed, a note will indicate the deletion.

Oversize materials (e.g., maps, drawings, charts) are reproduced by sectioning the original, beginning at the upper left-hand corner and continuing from left to right in equal sections with small overlaps.

Photographs included in the original manuscript have been reproduced xerographically in this copy. Higher quality 6" x 9" black and white photographic prints are available for any photographs or illustrations appearing in this copy for an additional charge. Contact UMI directly to order.

ProQuest Information and Learning
300 North Zeeb Road, Ann Arbor, MI 48106-1346 USA
800-521-0600

UMI®

Modeling and Control of a Flexible-Link Manipulator

Brandeen McDonald ©

August 14, 2001

A THESIS SUBMITTED IN PARTIAL FULFILLMENT OF THE REQUIREMENTS
OF THE MScEng DEGREE
IN
CONTROL ENGINEERING
FACULTY OF ENGINEERING
LAKEHEAD UNIVERSITY
THUNDER BAY, ONTARIO
CANADA

Abstract

The behaviour of a flexible-link robotic manipulator is studied using an experimental apparatus. The system is modeled based on the physical laws governing system dynamics. A non-linear rigid body model is developed which includes backlash and friction. Through comparison of experimental and simulation results, the small backlash in the system is shown to have little effect on the system behaviour.

Friction is shown to have a considerable effect on the system dynamics. The finite element method is used to develop a flexible body model for the flexible link. Experimental results show that the lateral vibration of the manipulator exhibits the behaviour of a clamped-free beam or a pinned-free beam during different stages of the motion. A combined dynamic model has been developed. The model is comprised of both a clamped-free beam model and a pinned-free beam model with the choice of model being determined by the boundary conditions at the hub that change due to the non-linear friction term included in the model.

Experimental and simulation results demonstrate that, at low speeds of rotation, the hub friction causes the pinned frequencies of vibration to approach the clamped frequencies. Vibration suppression controllers are considered based on the coupling torque from the clamped beam model. Different vibration-suppressing controllers are found to be effective in the pinned, high-speed region, the pinned, low-speed region and the clamped region. The effectiveness of vibration-suppressing controllers when added to a classical PD controller is studied.

Acknowledgements

I would like to thank Dr. K. Natarajan, my thesis supervisor, for providing direction and guidance. The attention to detail shown by Dr. K. Liu in his examination of the thesis was very helpful and much appreciated. The assistance and advice from Drs. A. Gilbert, K. Liu and M. Liu were sincerely appreciated. I would like to thank F. Briden and B. Misner for their help with the C programming language. My classmate Xiaodong Sun deserves thanks for his thoughtful discussion. Liz Tse deserves a special mention for her honest opinions. I am very grateful to Lori Kapush for proof reading this work. My heartfelt gratitude goes to my friends and family for their loving support, and not only believing I could do it, but also telling me so.

Table of Contents

List of Figures

List of Nomenclature

$\Delta\theta$ - the gear backlash width, in rad.
ϕ - the magnetic flux, in Vs.
$\phi_1(t), \phi_2(t), \phi_3(t)$ – generalized shape functions.
$\theta_1(x)$ – the slope of the beam at the hub, in rad.
$\theta_2(x)$ – the slope of the beam at the tip, in rad.
θ_a - the angle of the arm gear, in rad.
θ_m - the angle of the motor gear, in rad.
τ - the input to the rigid-flexible body system model.
τ_a - the torque supplied by the motor current, in Nm.
τ_l - the torque available to the motor load, in Nm.
τ_2 - the load torque on the arm gear side, in Nm.
ω_{a-} - arm speed before gear engagement, in rad/s.
ω_a - the arm speed, in rad/s.
ω_{a+} - arm speed after gear engagement, in rad/s.
ω_{m-} - motor speed before gear engagement, in rad/s.
ω_m - the motor speed in, rad/s.
ω_{m+} - motor speed after gear engagement, in rad/s.
A,B,C – the state space matrices.
a_0, a_1, a_2, a_3 – coefficients in the beam deflection equation.
b – the total viscous friction of the system in Nms
b_m – the viscous friction of the motor in Nms.
b_s – the viscous friction of the arm shaft in Nms.
B_T - the damping matrix for the combined rigid-flexible body system model.
D – gain of the derivative controller.
d_1 – the length of the counter balance, in m.
d_2 - the length of the flexible portion of the arm, in m.
d_3 – the distance to the payload, in m.
E – the modulus of elasticity for 6061-T6 aluminum, in Pa.
E_a – the back emf of the motor, in V.
f_1 - the force applied between gears due to torque τ_l, in N.
F_2 – generalized force on the tip of the beam, in N.
f_2 - the reaction force between the gears due to f_1, in N.
F_m – force at the tip of the beam due to $\ddot{\theta}_m$, in N.
F_M – the force on the end of the beam caused by a payload mass, in N.
I – the area moment of inertia of the arm, in m^4.
I – the identity matrix.
i_a – the current supplied to the motor, in A.
J – the total mass moment of inertia of the system, in kgm^2
J_a - the moment of inertia of the arm, arm shaft, arm gear and any payload, in kgm^2.
J_{g1} - the moment of inertia of the motor gear, in kgm^2.
J_{g2} - the moment of inertia of the arm gear and shaft, in kgm^2.

J_1 - the moment of inertia of the arm including payload, in kgm^2.
J_m - the moment of inertia of the motor and motor gear combined, in kgm^2.
J_{m2} – inertia of counterbalance, in kgm^2.
J_{m2} – the moment of inertia of the counterbalance, in kgm^2.
J_r - the moment of inertia of the motor (rotor), in kgm^2.
$k\phi$ - the motor constant in Nm/A.
K_B – generalized stiffness matrix.
k_{ij} – the elements of the generalized stiffness matrix, K_B.
K_{mo} – gain tuning parameter for vibration suppressing controller.
K_{SG} – gain used in calculating the second strain gage reading.
K_T - the stiffness matrix for the combined rigd-flexible body system model.
L – the length of the beam in m.
L_a – the motor inductance, in henrys
$M(x)$ – moment at any point along the beam, in Nm.
$m(x)$ – the per unit length mass of the beam, in kg/m.
M_1 – generalized moment at the hub, in Nm.
m_1 – the mass of the flexible portion of the arm, in kg.
M_2 – generalized moment on the tip of the beam, in Nm.
m_2 – the mass of the counter balance, in kg.
m_3 – the mass of the payload, in kg.
M_B – generalized mass matrix.
M_{BNo_mass} – M_B.
$M_{BPayload}$ – the generalized mass matrix for the system with payload.
m_{ij} – the elements of the generalized mass matrix, M_B.
M_m – torque at the tip of the beam due to $\ddot{\theta}_m$, in Nm.
M_o – reaction torque at the hub (referred to motor gear side) caused by the flexing of the arm, in Nm.
M_T – the mass matrix for the combined rigd-flexible body system model.
N – the gear ratio, r_1/r_2.
P - gain of the porportional controller.
$p(x)$ – the distributed force on the beam, in N/m.
Q – the input matrix for the combined rigd-flexible body system model.
r_1 - the radius of the motor gear, in m.
r_2 - the radius of the arm gear, in m.
R_a – the motor resistance, in ohms
SG – second strain gage reading, in V.
t – time, in seconds.
T_{af} - the arm shaft friction (coulomb and static), in Nm.
t_d – delay tuning parameter for vibration suppressing controller.
T_f - the total friction in the system, in Nm
T_{mf} - the motor friction (coulomb and static), in Nm.
u – the state input.
$v_2(x)$ – the deflection of the beam at the tip, in m.
x – the distance along the length of the beam, in m.
x – the state variable.
$y(x,t)$ – the deflection of the beam, in m.

Chapter 1

Introduction

1.1 Why Study Flexible Manipulators

The large mass and energy requirements of standard rigid link manipulators have led to a desire for flexible link manipulators characterized by low-mass links and actuators with low power requirements. This is particularly desirable in certain applications, such as space systems, where mass and energy requirements must be minimized for transport purposes. Flexible link dynamics are also found in certain mechanical pointing systems [18] and in systems with links having high length-to-width ratios. These dynamics make the system outputs such as tip position more difficult to control. If flexibility is not taken into account in controller design the system can become unstable. Therefore, before flexible link manipulators can be realistically implemented, it is necessary to study the nature of flexible link manipulators and determine effective methods for end-point position control.

1.2 Modeling of Robotic Arms

Studies on the modeling of flexible robotic arms can be divided into two areas – those that use identification based methods and those that develop models based on the physical laws of the dynamic system.

Identification based methods are advantageous in that they do not require specific system parameters and therefore can be used on systems that are already built and for which the governing equations are complex or system parameters are unknown and cannot be measured. However, in addition to large computation times, time domain identification based methods require a model order which can be difficult to choose as flexible body dynamics involve partial differential equations. The model order selected therefore usually results in over- or under- parameterization. Frequency domain methods have been used in [22] to avoid these problems associated with time domain identification models.

For systems that use the identified model for controller tuning, sufficient time must be available to update the model and tune the controller. It is shown in [23] that good performance results are obtained irrespective of payload using online identification and controller tuning. However, the identification and tuning of the controller is too time consuming to be practical. The FFT is used in [22] to reduce the identification time of the first natural frequency of the system. This mode is used to choose the controller gains in a gain scheduling technique. This significantly reduced the controller tuning time. Since addition of a payload tends to lower the first natural frequency, this method successfully adapts the controller to payload changes and provides good response to step inputs.

The majority of studies [8,12,5,2,7,9,3] based on the physics of the system use Lagrange's equation to construct a suitable state-space representation and include both rigid body and flexible body components. The energy balance nature of the Lagrangian method naturally includes coupling terms between the rigid and flexible bodies. In [3] however, the linear model is decoupled, and the coefficients of the state-space model are determined via an identification technique. An experimental technique is used in [11] to identify the frequencies of vibration. However, since it measures the beam vibrations after the arm has been rotated through a slew angle, it only measures the clamped-free frequencies [10]. Previous methods that use physical modeling techniques chose either clamped-free or pinned-free beam models for the flexible body, and use the corresponding eigenfunctions in the system model development. Results for both cases are compared in [9]. In [20] the eigenfunctions are chosen based on the frame of reference. This seems to imply that the frequency of vibration for a beam depends on the frame of reference. The frequency of vibration depends on the boundary conditions of the system, not the frame of reference. A different frame of reference for a model describing the same system should yield the same results.

In [12] the models from [9] are used and it is mentioned that a system with a higher hub inertia will have frequencies closer to the clamped-free frequencies and a system with lower hub inertia will have frequencies closer to the pinned-free frequencies. In [7, 6] the higher gear ratio reduces the effect of the oscillations of the arm on the motor and causes vibrations closer to the clamped mode. Such a high gear ratio also prevents a rapid response and therefore requires a motor with higher speed capabilities.

Some studies [5, 7] include terms to account for non-linearities such as Coulomb friction. In [7] the friction term is represented by a linear approximation.

Past studies [11,12,3,5,7] on flexible manipulators have used tip sensors to monitor the tip position and how it reacts to flexing. These include accelerometers that provide indirect estimation of tip position and video camera techniques that provide tip position for a limited range of movement. Other researchers [8, 9] have used strain gages to monitor the stress in the flexible link. In this case, when the sensor outputs have reached steady state, the tip position is equal to the hub position.

1.3 Control Strategies

Several different controller strategies have been studied in the literature. These include Linear quadratic regulator (LQR) [8,11,5], linear quadratic Gaussian (LQG) [12,3], acceleration feedback [11,23,22] root-locus design [11], feedforward [5,7], pole placement [7,2], gain adjustment [2], pole-zero cancellation [5], gain scheduling [22] and classical PD or PID [9,23]

LQR and LQG designs require a state-space linearized model of the system and rely on appropriate choices for the Q and R in the performance index. When full states are not available an observer is needed, which doubles the order of the system, increases computation time, and requires an accurate model.

Feedforward controllers also require an accurate system model. Linear models are only accurate for small changes about the point of linearization. Additionally, if the system is non-minimum phase, a pseudo-inverse needs to be calculated and used in order to obtain a stable controller.

Pole placement, while an easy tuning method, does not guarantee that the chosen poles will have low sensitivity as desired. Pole placement is ill suited for situations with varying payload as the desired closed loop poles may vary and may not be known in advance. Gain adjustment, can be time consuming and difficult to automate. It is a trial and error adjustment to find the feedback gains which yield good pole positions for the rigid and flexible bodies.

1.4 Thesis Overview

The contribution of this thesis is a dual model that combines clamped-free and pinned-free beam models for a single-link flexible manipulator, and leads to the design of a dual controller.

While hub inertias [12] and gear ratios can affect the frequency of vibration, there has been no mention in the literature that a flexible robotic manipulator system can exhibit both pinned and clamped frequencies when friction is taken into account and that both these cases must be considered when designing a controller, with a different controller used in each case to achieve vibration suppression. Static friction, a non-linear friction term can prevent the rotation of the hub, thereby changing the hub boundary condition from pinned to clamped. Also new in this thesis is that a system modeled using a pinned-free beam model can exhibit frequencies close to the clamped-free beam frequencies due to Coulomb friction in the system model and to that extent explains the behaviour observed in the physical system. Since Coulomb friction is a non-linear term, including this term in a boundary condition equation, similar to the hub inertia boundary condition equation in [12], would make solving the system equations difficult.

The model developed in this thesis is non-linear. It includes viscous, Coulomb, and static

friction. Both the rigid and the flexible bodies are modeled using the physical laws that govern the system. The equations for the rigid and flexible body motion are derived separately, and then combined. For the clamped model, an explicit reaction term [4,5] is added to couple the two systems. Modeling in this fashion, with an explicit reaction term, allows for the theoretical study of the nature of the coupling between the rigid and flexible bodies and allows for the design of a controller which can predict this coupling and reduce its effects on the system. An explicit coupling term cannot be determined for the pinned model. Since the nature of the coupling is different under pinned or clamped conditions, a dual controller is needed.

This thesis also uses strain gages to monitor beam flexing, but differs in that the gages are also used to predict the effects of flexing on the motor speed and the reaction torque at the hub. The effect of beam flexing on motor speed and arm position is important since these rigid body variables and the strain gage readings are the only values measured from the experimental system. While the majority of papers with experimental results [3,5,7,6,9,11,12,22,23] move the arm through angles ranging from 5 – 40 degrees, in this thesis, similar to [21], slew angles of 100 degrees are considered. Rotating the arm through a large angle allows a wider range of behaviours to be observed.

The outline of this thesis is as follows: Chapter 1 is the introduction. Chapter 2 develops the rigid body model of the system and explores the contribution of backlash to system dynamics. Chapter 3 develops the flexible body model of the system and describes the effects of friction. Chapter 4 shows the results for various control strategies and Chapter 5 gives conclusions and outlines future work.

Chapter 2

The System Under Study

The system under study is a single link, flexible manipulator. The experimental setup is shown in Figure 2.1. This arm is driven, through a set of gears, by a current-controlled dc motor. The current to the motor is provided through circuitry that accepts as inputs voltage signals representing the magnitude and direction of the current. These signals are the outputs of the digital controller, which is comprised of a computer and data acquisition board. Inputs to the controller are voltages proportional to arm shaft position and motor speed, as well as voltages provided by two strain gages mounted on the arm. One strain gage is mounted near the base of the arm (base gage), the other mounted approximately in the middle of the arm (second gage).

Flexible link manipulators are useful in that they are lightweight, therefore being easy to move and requiring less control effort. The disadvantage is that the link flexibility makes the end-point position more difficult to control, particularly in this case, since a direct sensor of tip position is not available. Instead, the strain gages are used to monitor the flexing of the arm. It is assumed that when the strain gage readings are zero the arm has stopped flexing and therefore, the tip position is directly related to the angular position of the hub as sensed at the arm joint by the position potentiometer.

The backlash and friction present in this system are non-linearities that can have a significant effect on the system behaviour and also make the system more difficult to control. Experiments show that much of the friction is due to the potentiometer used to sense the hub position (see Appendix A). The backlash is due to the imperfect meshing of the gears and can also occur when gears get worn down.

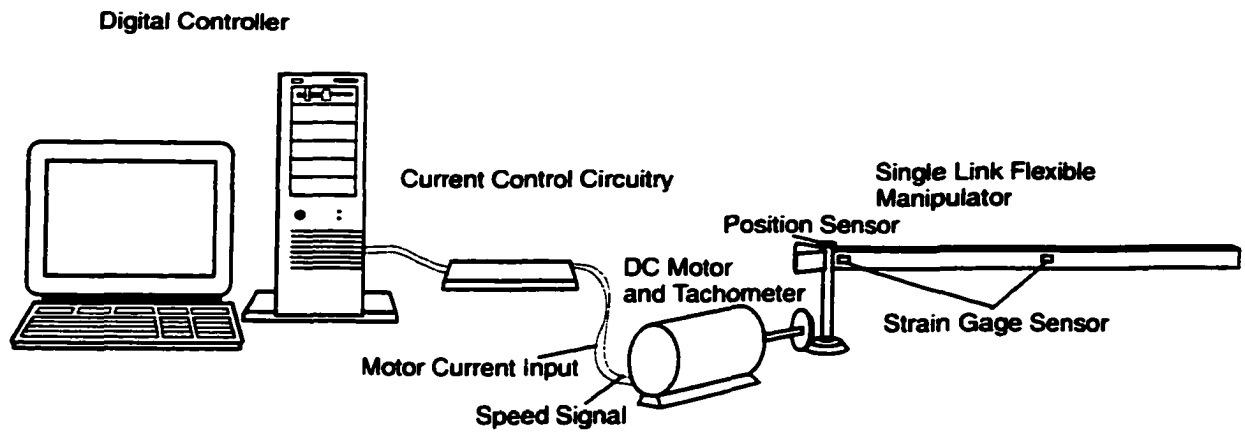

Figure 2.1 Experimental Setup

2.1 Rigid Body Model with Backlash and Friction

In this section the system is modeled as a rigid body, including the non-linearities of backlash and friction. The backlash width measures the maximum gap between motor gear teeth and arm gear teeth and as such, is the angle, in radians, subtended by the contact surfaces of the gear teeth at the centre of the motor gear.

To describe gear backlash, three cases must be described [18]: when the gears are engaged, when the gears are not engaged, and the moment of impact when the gears engage.

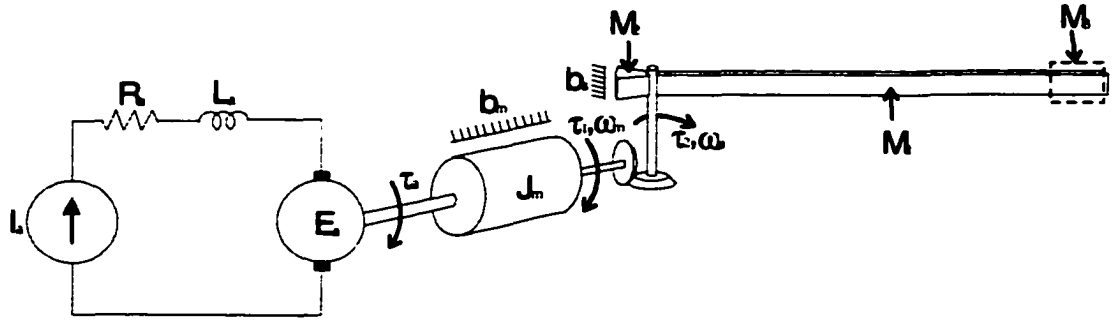

Figure 2.2 The flexible arm system.

When the gears are engaged, the system can be described by the general equation:

$$\tau_a = J\dot{\omega}_m + b\omega_m + T_f \qquad (2.1)$$

where $\tau_a = k\phi i_a$ is the torque (in Nm) supplied by the motor current, i_a (in A), k is a constant, ϕ is the magnetic flux (in Vs) [13], and J is the combined moment of inertia (in

kgm^2) of the motor, the gears, the arm and any mass supported by the arm. The variable, b, includes any viscous friction (in Nms). T_f is the effect of static and Coulomb friction, and ω_m is the angular motor speed.

We can derive Equation (2.1) from the system parameters shown in Figure 2.2. The torque available to the load, τ_1, is the driving motor torque minus the torque needed to overcome the viscous friction in the motor, b_m and the moment of inertia of the motor, J_r, and the motor gear, J_{g1}. With $J_m = J_r + J_{g1}$,

$$\tau_1 = \tau_a - J_m\dot{\omega}_m - b_m\omega_m - T_{mf}\,\mathrm{sgn}(\omega_m) \tag{2.2}$$

where

$$\mathrm{sgn}(\omega_m) = \begin{cases} 1, & \text{for } \omega_m > 0 \\ 0, & \text{for } \omega_m = 0 \\ -1, & \text{for } \omega_m < 0 \end{cases}$$

The load torque as provided by the moment of inertia of the arm, J_l, the viscous friction of the arm, b_s, and the moment of inertia of the arm-shaft gear, J_{g2}, must be referred to the motor-gear side before it can be substituted into Equation (2.2). The load torque on the arm-gear side is τ_2, as calculated in Equation (2.3)

$$\tau_2 = J_a\dot{\omega}_a + b_s\dot{\omega}_a + T_{af}\,\mathrm{sgn}(\omega_a) \tag{2.3}$$

where $J_a = J_l + J_{g2}$.

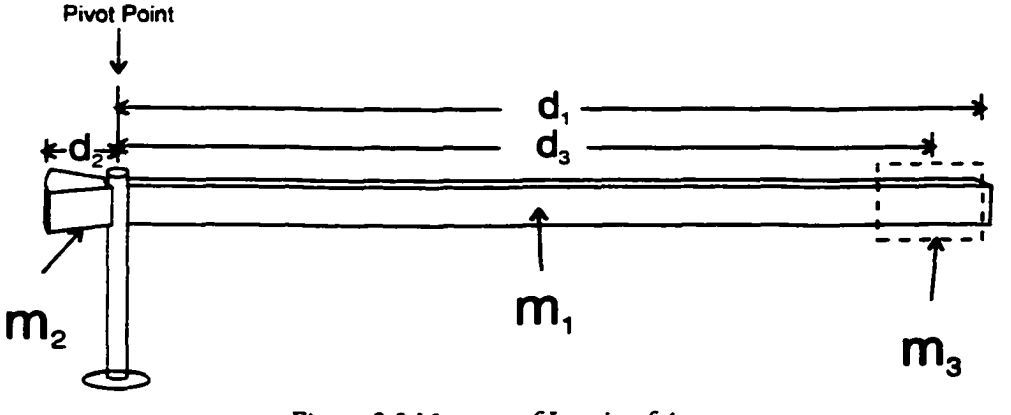

Figure 2.3 Moment of Inertia of Arm

From Figure 2.3, the moment of inertia of the arm about the pivot point is:

$$J_l = \frac{1}{3} m_1 d_1^2 + J_{m_2} + m_3 d_3^2 \qquad (2.4)$$

where

$$J_{m_2} = \frac{1}{3} m_2 d_2^2$$

is the moment of inertia of the counterbalance, and m_1, m_2 and m_3 are the mass of the arm, counterbalance and payload respectively.

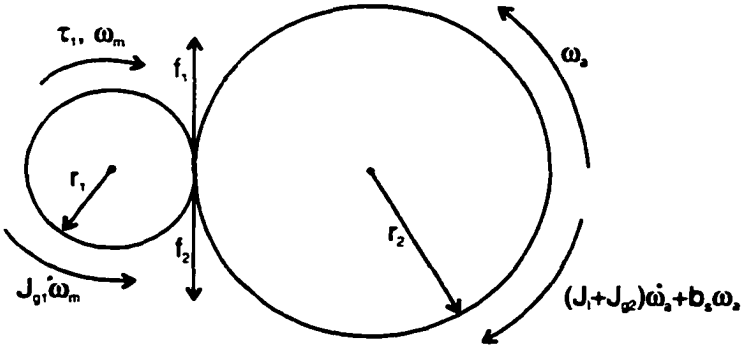

Figure 2.4 Forces and torques acting on the gears.

Figure 2.4 illustrates the forces and torques acting on the gears. Gear 1, the motor gear, is driven by a torque, τ_1, at a speed, ω_m. This applied torque provides a force, f_1. An equal and opposite force, f_2, reacts to f_1 and drives gear 2, the arm shaft gear, providing a torque equal to $r_2 f_2$. This torque, τ_2, overcomes the combined moment of inertia of the arm and gear 2, and causes gear 2 to rotate at speed ω_a. This is represented mathematically by Equations (2.5), (2.6) and (2.7).

$$\tau_1 = r_1 f_1 \qquad (2.5)$$

$$\tau_2 = r_2 f_2 = J_a \dot{\omega}_a + b_s \omega_a + T_{af}\,\mathrm{sgn}(\omega_a) \qquad (2.6)$$

$$f_1 = f_2 \qquad (2.7)$$

Substituting Equations (2.5) and (2.6) into Equation (2.7) we get:

$$\tau_1 = \frac{r_1 \tau_2}{r_2}$$

and further substituting for τ_2 we get:

$$\tau_1 = \frac{r_1}{r_2}\left[J_a\dot{\omega}_a + b_s\omega_a + T_{af}\,\mathrm{sgn}(\omega_a)\right] \tag{2.8}$$

Now the linear velocities of the two gears must be equal, *i.e.*, the same circumferential distance is covered by the two gears in the same amount of time. That is:

$$r_1\omega_m = r_2\omega_a\,. \tag{2.9}$$

Therefore, the angular speed of gear 2 is related to gear 1 by Equation (2.10).

$$\omega_a = \frac{r_1}{r_2}\omega_m \tag{2.10}$$

Substituting Equation (2.10) into Equation (2.8) gives an equation in terms of motor speed.

$$\tau_1 = \left(\frac{r_1}{r_2}\right)^2\left[J_a\dot{\omega}_m + b_s\omega_m\right] + \left(\frac{r_1}{r_2}\right)T_{af}\,\mathrm{sgn}(\omega_m)\,. \tag{2.11}$$

Substituting this result into Equation (2.2) gives:

$$\tau_a = \tau_1 + J_m\dot{\omega}_m + b_m\omega_m + T_{mf}\,\mathrm{sgn}(\omega_m), \tag{2.12}$$

and

$$\tau_a = J\dot{\omega}_m + b\omega_m + T_f, \quad \text{where}$$

$$J = J_m + \left(\frac{r_1}{r_2}\right)^2 J_a$$

$$b = b_m + \left(\frac{r_1}{r_2}\right)^2 b_s \quad \text{and}$$

$$T_f = T_{mf}\,\mathrm{sgn}(\omega_m) + \left(\frac{r_1}{r_2}\right)T_{af}\,\mathrm{sgn}(\omega_m)$$

Although the gear backlash width, measured in radians, does not appear in the general system equation, Equation (2.1), the backlash must be considered when solving the equations for motor angle and arm angle. There are two cases to consider: when the motor is moving in the direction of positive speed and when the motor is moving in the direction of negative speed. If an angle reference is chosen such that when the motor is

turning in the positive direction, the arm position is $\theta_a = (\theta_m)\frac{r_1}{r_2}$. Then, when the gears are engaged in the direction of negative speed, the arm position is $\theta_a = (\theta_m + \Delta\theta)\frac{r_1}{r_2}$ due to gear backlash of width $\Delta\theta$ radians.

When the gears are not engaged the arm and motor develop speeds separately. The motor torque only has to overcome the motor friction, and the motor and motor gear inertia, as shown in Equation (2.13). The arm is developing speed according to Equation (2.14) where T_{af} is the torque due to static and Coulomb friction.

$$\tau_a = J_m\dot{\omega}_m + b_m\omega_m + T_{mf}\,\mathrm{sgn}(\omega_m) \tag{2.13}$$

$$0 = J_a\dot{\omega}_a + b_s\omega_a + T_{af}\,\mathrm{sgn}(\omega_a) \tag{2.14}$$

At the moment that the two gears engage, a momentum transfer occurs. From Figure 2.4 we can see that at the moment the gears engage, two equal and opposite forces are present at the point of contact. As shown below, the integral of the torque caused by these forces, represents the change in angular momentum of the respective body.

$$\int_{t-}^{t+} r_1 \times f_1 dt = J_m\omega_{m+} - J_m\omega_{m-} \tag{2.15}$$

$$\int_{t-}^{t+} r_2 \times f_2 dt = J_a\omega_{a+} - J_a\omega_{a-} \tag{2.16}$$

Since the forces are perpendicular to the radius of rotation, the cross product on the right hand side of Equations (2.15) and (2.16) reduces to a scalar product and the radius can be brought outside the integral.

$$r_1\int_{t-}^{t+} f_1 dt = J_m\omega_{m+} - J_m\omega_{m-} \tag{2.17}$$

$$r_2\int_{t-}^{t+} f_2 dt = J_a\omega_{a+} - J_a\omega_{a-} \tag{2.18}$$

Since the forces have equal magnitudes but opposite directions, the integrals in Equations (2.17) and (2.18) sum to zero and adding the two equations gives:

$$\frac{J_m\omega_{m+} - J_m\omega_{m-}}{r_1} = \frac{-J_a\omega_{a+} + J_a\omega_{a-}}{r_2}$$

which can be rearranged to

$$\omega_{m+} = \frac{J_m \omega_{m-} + \left(\frac{r_1}{r_2}\right) J_a \omega_{a-}}{J_m + J_a \left(\frac{r_1}{r_2}\right)^2} \tag{2.19}$$

where $\omega_{a+} = \left(\frac{r_1}{r_2}\right) \omega_{m+}$.

In the direction of positive speed, the gears will engage when:

$$\theta_m = \frac{r_2}{r_1}\theta_a \text{ and } \dot{\theta}_m > \frac{r_2}{r_1}\dot{\theta}_a \text{ or } \ddot{\theta}_m > \frac{r_2}{r_1}\ddot{\theta}_a . \tag{2.20}$$

In the direction of negative speed, the gears will engage when:

$$(\theta_m + \Delta\theta) = \frac{r_2}{r_1}\theta_a \text{ and } \dot{\theta}_m < \frac{r_2}{r_1}\dot{\theta}_a \text{ or } \ddot{\theta}_m < \frac{r_2}{r_1}\ddot{\theta}_a . \tag{2.21}$$

The gears will disengage when:

$$(\omega_{m-})(\omega_{a-}) > 0 \text{ and } (\omega_{m-})(\omega_{m+}) < 0 \quad \text{or} \quad (\omega_{a-})(\omega_{a+}) < 0 . \tag{2.22}$$

2.2 Friction Model

Figure 2.5 shows the friction model used in this thesis [1]. The static friction occurs when the speed is zero and opposes any applied torque until the value of that torque exceeds the static friction limit. The static friction then remains constant at this limit. The Coulomb friction occurs when speed is not zero and acts in an opposing direction to the direction of motion. The viscous friction is proportional to the speed and is the *b* term in Equation (2.1).

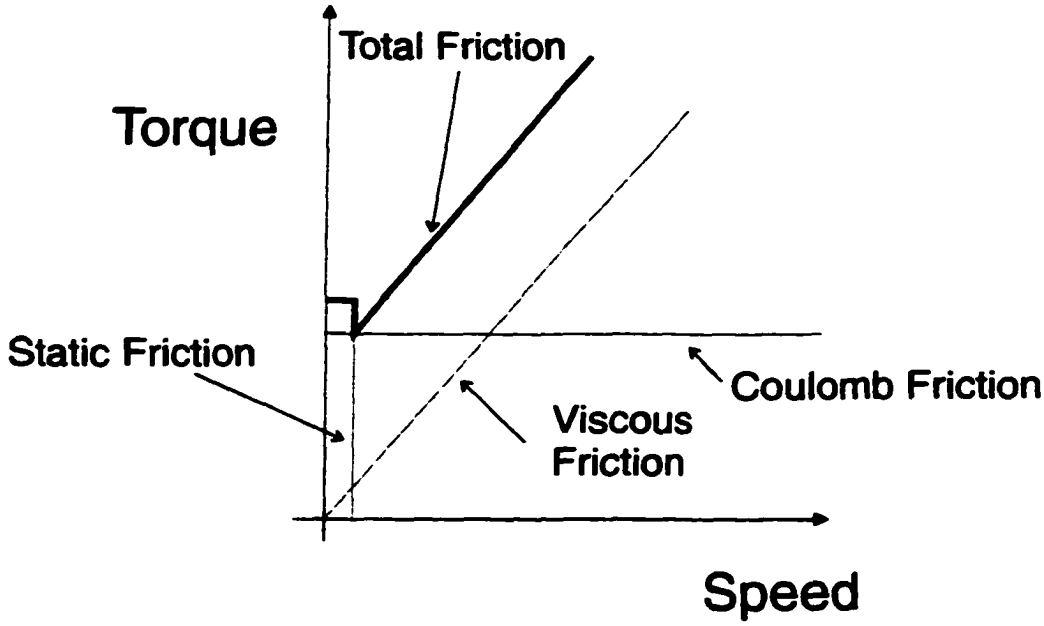

Figure 2.5 Friction Model

2.3 Comparison of Simulated and Experimental Data

The system was simulated with the following system constants:

SYSTEM CONSTANTS USED IN SIMULATIONS	
$J_m = 0.00193$ kgm^2	$r_1 / r_2 = 1/N = 1/1.5$
$T_{mf} = 0.066$ Nm (Coulomb)	$b_m = 0.0008$ Nms
$= 0.09487$ Nm (static)	$b_s = 0.1$ Nms
$T_{af} = 0.183$ Nm (Coulomb)	$m_3 = 0$ kg
$= 0.21574$ Nm (static)	$d_3 = 1$ m
$J_a = 0.158 + m_3 d_3^2$ kgm^2	$\Delta\theta = 0.01164$ rad
$J_{m2} + J_{g2} = 0.00129$ kgm^2	

Table 2.1 Values for system constants used in simulations.

These values were determined experimentally through experiments on the flexible arm system, as a whole, and on the dc motor separately (see Appendix A).

The system setpoint is a 0.2 Hz square wave that oscillates between ±50 degrees. A square wave input is chosen so that the system response can be observed as the arm changes direction of rotation, causing the engaged gears to disengage before engaging again. A Proportional controller with velocity feedback (PD control) is used in both simulation and experimental systems. The gains P=2.5308 and D=0.6625 were determined from the open loop frequency response of the experimental system using

Ziegler-Nichols tuning rules. Figure 2.6 shows the setpoint, position, motor speed, and control effort for the experimental and simulated system.

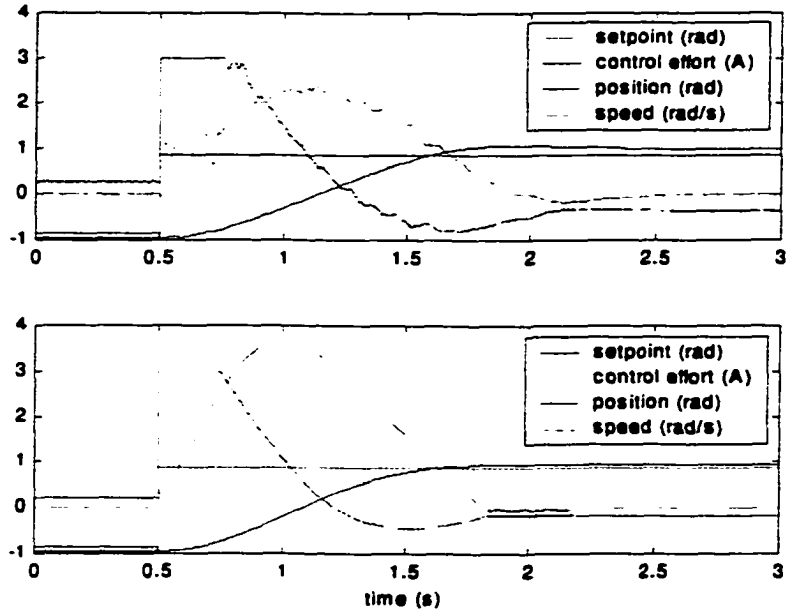

Figure 2.6 Experimental (top) and simulated (bottom) results. Controller settings P=2.5308, D = 0.6625. Simulation has backlash and friction.

Although the simulation adequately models the position, the simulation fails to exhibit the behaviour shown in the experimental speed. The simulated speed only shows a minor jump at the setpoint bump, which is caused by the backlash in the simulation. To illustrate that this jump in the simulation is caused by backlash, Figure 2.7 shows the experimental speed along with the simulated speed with backlash included and with backlash excluded.

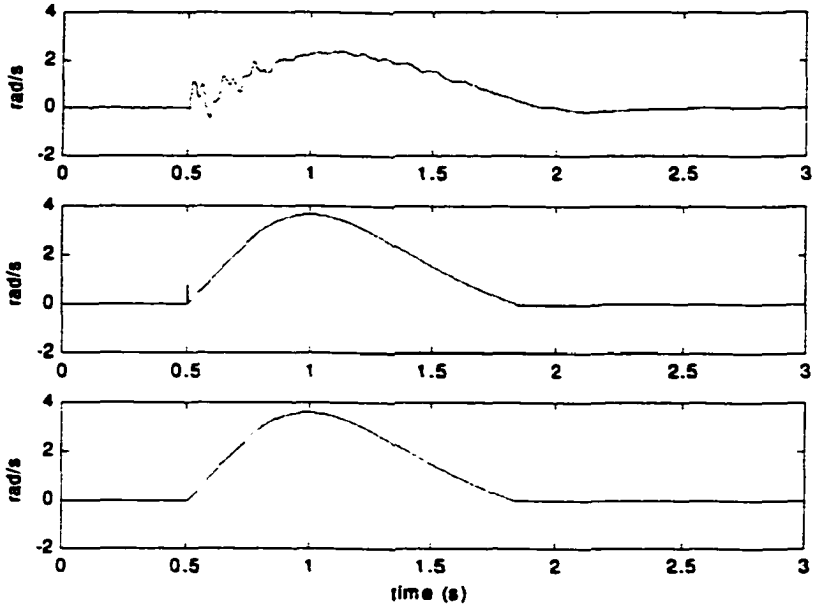

Figure 2.7 Experimental Speed, Simulated speed with backlash, Simulated Speed without backlash.

As can be seen in Figure 2.7, the simulated system without backlash does not show a jump in speed at the setpoint bump. The question remains as to whether the jump in speed in the experimental results is due to backlash. To determine this, the same controller was applied except a limit was placed on the rate of change of the control effort. Therefore the control effort would ramp up instead of step up. The speed results for the experimental system and the simulated system with and without backlash are shown in Figure 2.8.

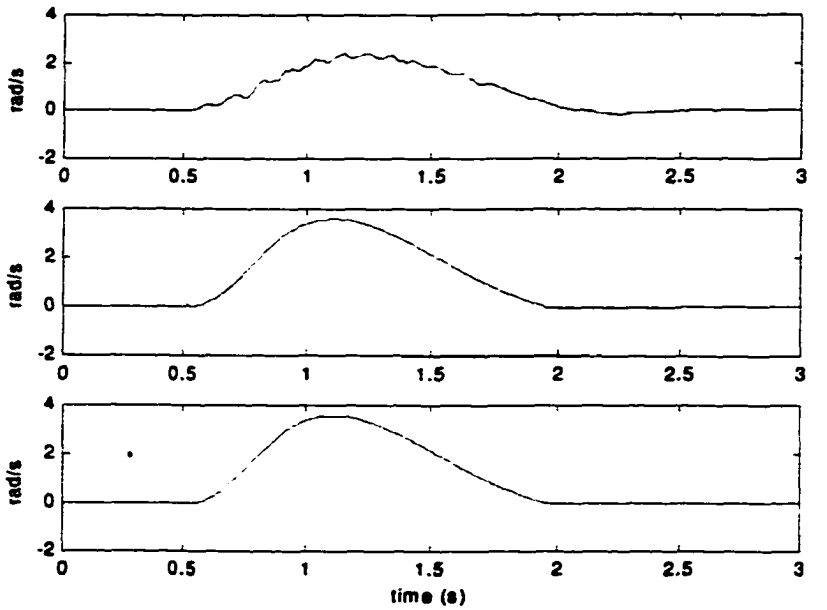

Figure 2.8 Experimental Speed, Simulated speed with backlash, Simulated speed without backlash. Controller rate has been constrained.

The experimental system no longer shows a huge jump in speed. Oscillations are still present in the speed, however. For the simulated system with backlash a jump in speed is still visible although it is smaller. The simulated system never shows oscillations in the speed. Additionally, were the jump in speed in the experimental system of Figure 2.7 (controller not constrained) due to backlash, the system would also show a jump in speed when the speed crossed the zero axis (*i.e.* the arm changed direction) at about 2 s; however it does not. Therefore we can conclude that backlash has little discernible effect on this system. This is likely due to the fact that the backlash is small (less than one degree) and the friction in the system is quite large.

2.4 Effects of Flexing on Speed

Figure 2.9 is a plot of the experimental results from Figure 2.6 and shows the speed, the base gage reading and the second gage reading. It can be seen that the oscillatory behaviour in the speed is a delayed version of the oscillatory behaviour exhibited by the second gage. This is significant because the second strain gage monitors beam flexing; therefore the flexing of the beam is affecting the motor speed. The shape of the base gage measurement exhibits the oscillatory behaviour of the second gage measurement, and additionally, has a strong resemblance to the control effort (this is also shown in Figure 4.20 and Figure 4.21). This is expected since both the beam flexing and the control torque will put strain on the beam at the hub.

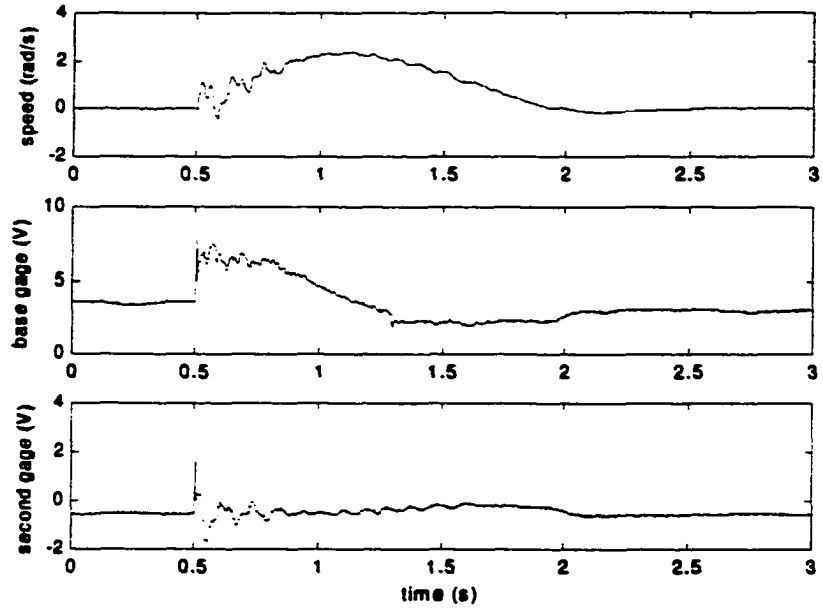

Figure 2.9 Experimental Speed, Base Gage and Second Gage Measurements

The experimental results show that there is coupling between the motion of the hub and the arm, and the flexing of the arm and the hub speed, and thereby demonstrate that the flexible arm dynamics have a significant effect on the total system dynamics. The simulation results show that the system behaviour is not accurately modeled when the flexible arm dynamics are not included in the model, although the backlash has been included. Simulation result in Chapter 3 will show that a model that includes the flexible arm dynamics, while omitting backlash, adequately models the system behaviour.

2.5 Conclusions

Simulation of the system, as a rigid body only, demonstrates that the small backlash present has very little effect on the system dynamics. The remaining significant nonlinearities in the system are Coulomb and static friction. Chapter 3 considers the effects of these nonlinearities on system behaviour.

The next chapter models the flexible behaviour of the arm and combines the flexible body and rigid body dynamics into one coupled system. Friction is included in the model. However, backlash is not. The results in the next chapter will reinforce that backlash can be neglected for this system.

Chapter 3

System Model Combining Rigid Body and Flexible Arm Dynamics

An appropriate beam model for the flexible arm must be chosen based on the boundary conditions at the ends of the arm. These boundary conditions describe constraints on the ends of a beam, such as whether a beam is free to rotate or not. For different boundary conditions the beam will vibrate at different frequencies [10]. Previous studies choose either clamped-free or pinned-free boundary conditions for the beam model. This thesis shows that a system with friction can exhibit both pinned-free and clamped-free behaviour due to a change in boundary conditions. The changing nature of these boundary conditions can be observed in the system behaviour. Figure 3.1 shows the speed and second gage response of the system to a PD controller. The important characteristic shown is that when the speed is zero the flexing occurs at a frequency of 2 Hz instead of 10 Hz. This change in frequency is due to the friction in the system. Due to the low hub inertia, when the control effort is large enough to overcome the static friction in the system, the arm is able to rotate at the hub and the arm exhibits pinned-free beam behaviour vibrating at a frequency of 10 Hz. This oscillation is also transferred to the speed. When the friction is too great to be overcome by the total torque at the hub, the hub speed is zero. Since the hub cannot rotate, due to friction, the arm then acts like a clamped-free beam oscillating at 2Hz, where the oscillation occurs due to the initial deflection and momentum of the arm when it enters this clamped mode. Theoretically, based on the physical dimensions of the beam, the pinned and clamped frequencies of vibration would be 10.6 Hz and 2.4 Hz respectively, if hub inertia were not taken into account. Hub inertia lowers the frequency of vibration. No vibration is seen in the speed, in the clamped-free mode, since any coupling torque is not large enough to overcome the static friction forces, although the arm continues to flex.

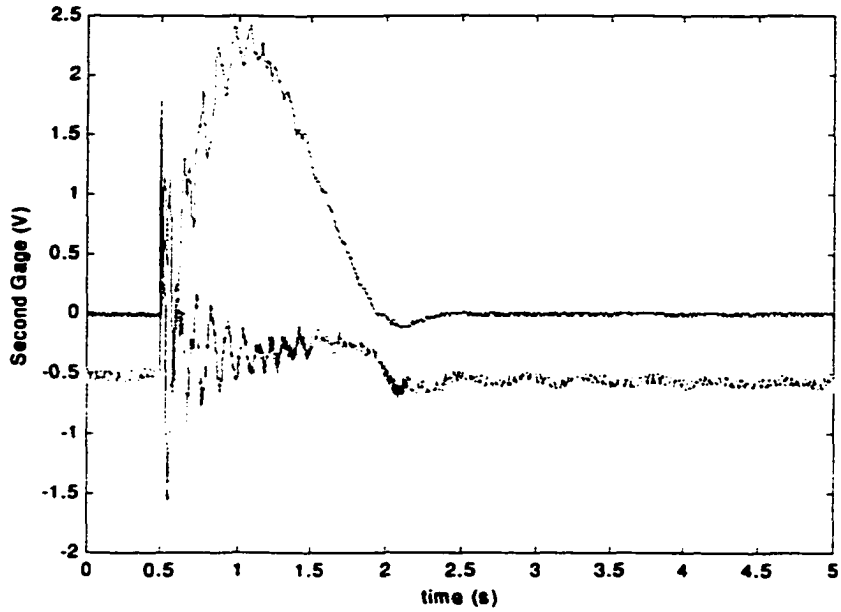

Figure 3.1 Experimental Second Gage (V) (green) and Speed (rad/s) (blue) for system with no payload

Therefore, two different beam models must be used in modeling the flexible arm portion of the system – a clamped-free model, and a pinned-free model. The beam models will combine with the rigid body system in different ways – the clamped model will use an explicit coupling term while the pinned model does not. A combined rigid-flexible body model must be determined for both the pinned and the clamped cases. The boundary conditions of the simulation will then determine when each model is used.

The flexible body dynamics of the system refer to the deflection of the beam from the expected rigid body position. The equations for this motion can be determined using the Lagrange equations and the assumed modes method [19]. If the deflection is assumed to be the sum of the generalized coordinates multiplied by shape functions, the equations can be determined by computing the generalized mass, generalized stiffness, generalized force, and generalized moment. The generalized coordinates and shape functions can be determined using the finite-element method. This is less labour intensive than solving the Euler-Bernoulli beam equation, which is a fourth order partial differential equation [9]. Also, system constants such as hub inertia and payload mass must be included in the boundary conditions when solving the partial differential equation. Thus for any changes in these values the equations must be re-solved before a model can be obtained. In the finite-element method this is not necessary and in the resulting total system such values can be updated directly if they change. This is advantageous when modeling a system with varying payload, especially if the model will be used for real-time control.

3.1 Pinned-Free Beam Model

For simplicity, the beam is modeled as a single finite element. This is adequate since the system behaviour is dominated by the first mode, which is a relative simple shape function [19]. If a pinned-beam is modeled as a single finite element, there are three generalized (independent) coordinates: slope of the beam at the hub, θ_1, the tip deflection, v_2 and the tip slope θ_2. The deflection of the beam at any point along its length is then:

$$y(x,t) = \theta_1(t)\phi_1(x) + v_2(t)\phi_2(x) + \theta_2(t)\phi_3(x) \tag{3.1}$$

where ϕ_1, ϕ_2 and ϕ_3 are the shape functions and x is the distance along the beam. θ_1, v_2 and θ_2 are functions of time only, and ϕ_1, ϕ_2 and ϕ_3 are functions of space only (distance, x).

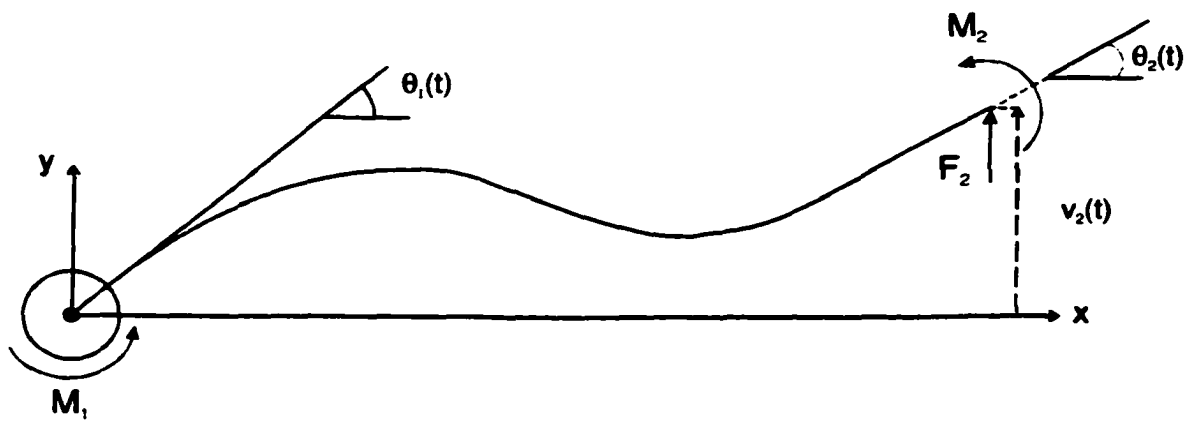

Figure 3.2 Beam Deflection in the x-y plane.

The generalized mass, M_B and generalized stiffness, K_B, are determined from these shape functions [19]. Knowing these values as well as the generalized forces, M_1, M_2 and F_2, the equation for the flexible body system is:

$$M_B\begin{bmatrix}\ddot{\theta}_1\\ \ddot{v}_2\\ \ddot{\theta}_2\end{bmatrix} + K_B\begin{bmatrix}\theta_1\\ v_2\\ \theta_2\end{bmatrix} = \begin{bmatrix}M_1\\ F_2\\ M_2\end{bmatrix} \tag{3.2}$$

The shape functions must be chosen to satisfy the boundary conditions of the system. For the case of a pinned-free beam the boundary conditions are:

$$\begin{aligned} y(0,t) &= 0 \qquad y(L,t) = v_2 \\ y'(0,t) &= \theta_1 \qquad y'(L,t) = \theta_2 \end{aligned} \tag{3.3}$$

The beam deflection at any time is chosen to be a third-order polynomial in x since this is the lowest order polynomial that can be a solution to the fourth order homogeneous Euler-Bernoulli beam equation. If the beam deflection is chosen as:

$$y(x,t) = a_3 x^3 + a_2 x^2 + a_1 x + a_0 \tag{3.4}$$

Then based on the boundary conditions, the constants are found to be:

$$\begin{aligned} a_0 &= 0 \\ a_1 &= \theta_1 \\ a_2 &= -\frac{2}{L}\theta_1 + \frac{3}{L^2}v_2 - \frac{\theta_2}{L} \\ a_3 &= \frac{1}{L^2}\theta_1 - \frac{2}{L^3}v_2 + \frac{\theta_2}{L^2} \end{aligned} \tag{3.5}$$

Substituting these constants into Equation (3.4) and rearranging gives:

$$\begin{aligned} y(x,t) &= \theta_1(t)\underbrace{\left(x - \frac{2x^2}{L} + \frac{x^3}{L^2}\right)}_{\phi_1} + v_2(t)\underbrace{\left(\frac{-2x^3}{L^3} + \frac{3x^2}{L^2}\right)}_{\phi_2} + \theta_2(t)\underbrace{\left(\frac{x^3}{L^2} - \frac{x^2}{L}\right)}_{\phi_3} \\ y(x,t) &= \theta_1(t)\phi_1(x) + v_2(t)\phi_2(x) + \theta_2(t)\phi_2(x) \end{aligned} \tag{3.6}$$

The generalized mass matrix [19] is given by:

$$M_B = [m_{ij}] \qquad \text{where } m_{ij} = \int_0^L m(x)\phi_i\phi_j dx \tag{3.7}$$

where $m(x)$ is the mass per unit length on the beam (assumed to be constant, *i.e.* $m(x) = m$).

The generalized stiffness matrix [19] is given by:

$$K_B = [k_{ij}] \qquad \text{where } k_{ij} = \int_0^L EI\phi_i\phi_j dx \tag{3.8}$$

where E is the modulus of elasticity for 6061-T6 Aluminum Alloy and I is the area moment of inertia of the arm.

For the pinned system, the torque at the hub causes the movement of the arm that leads to a change in θ_1 and the subsequent beam vibration. From the rigid body equations in Section 2.1 the torque at hub in terms of motor gear angle is:

$$\tau_{hub} = M_1 = N\left[\tau_a - J_m\ddot{\theta}_m - b_m\dot{\theta}_m - T_{mf}\,\mathrm{sgn}(\dot{\theta}_m)\right] - b_s\frac{\dot{\theta}_m}{N} - (J_{M2} + J_{g2})\frac{\ddot{\theta}_m}{N} - T_{af}\,\mathrm{sgn}(\dot{\theta}_m)$$

The only force acting on the beam is a torque applied at the hub. Therefore,

$$\begin{aligned} M_1 &= N\left[\tau_a - J_m\ddot{\theta}_m - b_m\dot{\theta}_m - T_{mf}\,\mathrm{sgn}(\dot{\theta}_m)\right] - b_s\frac{\dot{\theta}_m}{N} - (J_{M2} + J_{g2})\frac{\ddot{\theta}_m}{N} - T_{af}\,\mathrm{sgn}(\dot{\theta}_m) \\ F_2 &= 0 \\ M_2 &= 0 \end{aligned} \tag{3.9}$$

The moment, M_1, is the equation that links the rigid body to the flexible body. Since the arm angle is related to the motor angle through the gear ratio, the substitution $\theta_1 = \theta_m/N$ is made in Equation (3.2), and the resulting system has the state variables θ_m, v_2, and θ_2.

Therefore, the dynamic equation for the combined rigid-flexible body system is:

$$M_T\begin{bmatrix}\ddot{\theta}_m \\ \ddot{v}_2 \\ \ddot{\theta}_2\end{bmatrix} + B_T\begin{bmatrix}\dot{\theta}_m \\ \dot{v}_2 \\ \dot{\theta}_2\end{bmatrix} + K_T\begin{bmatrix}\theta_m \\ v_2 \\ \theta_2\end{bmatrix} = Q\tau$$

where

$$M_T = \begin{bmatrix} M_{B11} + NJ_m + \dfrac{(J_{M2} + J_{g2})}{N} & M_{B12} & M_{B31} \\ M_{B21} & M_{B22} & M_{B32} \\ M_{B31} & M_{B23} & M_{B33} \end{bmatrix} \quad B_T = \left[\begin{array}{c|c} Nb_m + \dfrac{b_s}{N} & 0_{1x2} \\ \hline 0_{2x1} & 0 \end{array}\right]$$

$$K_T = K_B \qquad Q = \begin{bmatrix}1\\0\\0\end{bmatrix} \qquad \tau = N\tau_a - T_f \qquad T_f = NT_{mf}\,\mathrm{sgn}(\dot{\theta}_m) + T_{af}\,\mathrm{sgn}(\dot{\theta}_m)$$

$$M_B = \frac{mL}{420}\begin{bmatrix} 4L^2 & 13L & -3L^2 \\ 13L & 156 & -22L \\ -3L^2 & -22L & 4L^2 \end{bmatrix} \quad K_B = \frac{EI}{L^3}\begin{bmatrix} 4L^2 & -6L & 2L^2 \\ -6L & 12 & -6L \\ 2L^2 & -6L & 4L^2 \end{bmatrix}$$

These equations are written in state-space format as:

$$\dot{x} = Ax + Bu$$
$$y = Cx \tag{3.10}$$

$$\text{where } x = \begin{bmatrix} \theta_m \\ v_2 \\ \theta_2 \\ \dot{\theta}_m \\ \dot{v}_2 \\ \dot{\theta}_2 \end{bmatrix}, \quad y = \begin{bmatrix} \theta_a \\ v_2 \\ \theta_2 \\ \dot{\theta}_m \\ \dot{v}_2 \\ \dot{\theta}_2 \end{bmatrix} \text{ and } u = \tau = N\tau_a - T_f. \tag{3.11}$$

$$A = \left[\begin{array}{c:c} 0 & I \\ \hdashline M_T^{-1}K_T & M_T^{-1}B_T \end{array}\right] \tag{3.12}$$

$$B = \left[\begin{array}{c} 0 \\ \hdashline M_T^{-1}Q \end{array}\right], \text{ and } C = \begin{bmatrix} 1/N & 0 & 0 & 0 & 0 & 0 \\ 0 & 1 & 0 & 0 & 0 & 0 \\ 0 & 0 & 1 & 0 & 0 & 0 \\ 0 & 0 & 0 & 1 & 0 & 0 \\ 0 & 0 & 0 & 0 & 1 & 0 \\ 0 & 0 & 0 & 0 & 0 & 1 \end{bmatrix}. \tag{3.13}$$

A payload mass acts as a force on the end of the beam, F_M, where $F_M = -m_3\ddot{v}_2$. To include a payload in the calculations, only the mass matrix, M_B of the flexible body equations changes such that:

$$M_{BPayload} = M_{BNo\_mass} + \begin{bmatrix} 0 & 0 & 0 \\ 0 & m_3 & 0 \\ 0 & 0 & 0 \end{bmatrix}. \tag{3.14}$$

It should be noted that although Equation (3.10) appears linear, due to the dependence of u on $\text{sgn}(\dot{\theta}_m)$ through T_f, this equation is nonlinear.

3.2 Clamped-Free Beam Model

For the clamped-free beam modeled as a single finite element, there are only two generalized (independent) coordinates: the tip deflection, v_2 and the tip slope θ_2. The

deflection of the beam at any point along its length is then:

$$y(x,t) = v_2(t)\phi_1(x) + \theta_2(t)\phi_2(x) \tag{3.15}$$

where ϕ_1 and ϕ_2 are the shape functions and x is the distance along the beam. Note that v_2 and θ_2 are functions of time only, and ϕ_1 and ϕ_2 are functions of space only.

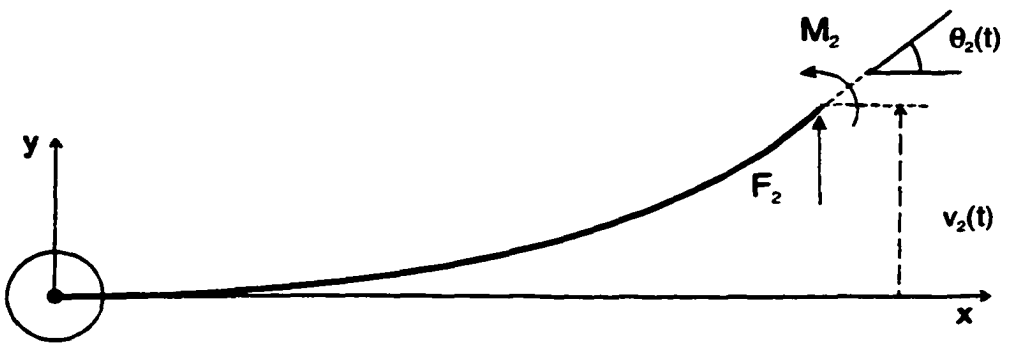

Figure 3.3 Beam Deflection in the x-y plane.

The generalized mass, M_B and generalized stiffness, K_B, are determined from these shape functions. Knowing these values as well as the generalized forces, M_2 and F_2, the equation for the flexible body system is:

$$M_B\begin{bmatrix}\ddot{v}_2\\ \ddot{\theta}_2\end{bmatrix} + K_B\begin{bmatrix}v_2\\ \theta_2\end{bmatrix} = \begin{bmatrix}F_2\\ M_2\end{bmatrix} \tag{3.16}$$

The shape functions must be chosen to satisfy the boundary conditions of the system. For the case of a clamped-free beam the boundary conditions are:

$$\begin{aligned} y(0,t) &= 0 \qquad y(L,t) = v_2 \\ y'(0,t) &= 0 \qquad y'(L,t) = \theta_2 \end{aligned} \tag{3.17}$$

If, as in Section 3.1, the beam deflection at any time is chosen to be a third-order polynomial in x:

$$y(x,t) = a_1x^3 + a_2x^2 + a_3x + a_4 \tag{3.18}$$

then based on the boundary conditions, the constants evaluate to:

$$a_4 = a_3 = 0$$
$$a_2 = \frac{3}{L^2} v_2 - \frac{\theta_2}{L} \tag{3.19}$$
$$a_1 = \frac{-2}{L^3} v_2 + \frac{\theta_2}{L^2}$$

Substituting these constants and rearranging gives:

$$y(x,t) = v_2(t)\underbrace{\left(\frac{-2x^3}{L^3} + \frac{3x^2}{L^2}\right)}_{\phi_1} + \theta_2(t)\underbrace{\left(\frac{x^3}{L^2} - \frac{x^2}{L}\right)}_{\phi_2} \tag{3.20}$$
$$y(x,t) = v_2(t)\phi_1(x) + \theta_2\phi_2$$

The generalized mass matrix is given by:

$$M_B = \lfloor m_{ij} \rfloor \quad \text{where } m_{ij} = \int_0^L m(x)\phi_i\phi_j dx \tag{3.21}$$

The generalized stiffness matrix is given by:

$$K_B = \lfloor k_{ij} \rfloor \quad \text{where } k_{ij} = \int_0^L EI\phi_i\phi_j dx \tag{3.22}$$

For the combined system, the loading on the clamped beam is caused by the accelerating hub. The acceleration of the hub, $\ddot{\theta}_a$, causes a distributed force on the beam, *p(x)*, which can be represented by a force and a moment at the tip of the beam, F_2 and M_2. These can be calculated from the generalized force equations:

$$F_2 = \int_0^L p(x)\phi_1(x)dx$$
$$M_2 = \int_0^L p(x)\phi_2(x)dx \tag{3.23}$$

where $p(x) = -m\ddot{\theta}_a x$ is the distributed force on the beam [19,17].

$$F_2 = \frac{-7mL^2}{20}\ddot{\theta}_a = \frac{-7mL^2}{20(N)}\ddot{\theta}_m = F_m\ddot{\theta}_m$$
(3.24)

$$M_2 = \frac{mL^3}{20}\ddot{\theta}_a = \frac{mL^3}{20(N)}\ddot{\theta}_m = M_m\ddot{\theta}_m \tag{3.25}$$

where $F_m = \frac{-7mL^2}{20(N)}$ and $M_m = \frac{mL^3}{20(N)}$.

Figure 3.4. Positive direction of reaction torque, M_o at the hub caused by flexing of the arm due to applied torque τ_l.

Figure 3.4 illustrates the positive direction of the torque acting on the hub (M_o) [16] due to the flexing of the beam when a torque of τ_l has been applied to the hub. Note that for the deflection shown in Figure 3.4 the value of M_o will be negative since it opposes the applied torque. The variables τ_l, ω_m, and Mo act on the motor side of the gears.

The moment at any point along the arm can be found from:

$$M(x) = EIy''(x,t)$$

The equation for the rigid body can now be changed to:

$$\tau_a + M_o = J\ddot{\theta}_m + b\dot{\theta}_m + T_f \tag{3.26}$$

$$\text{with } M_o = \frac{M(0)}{N} = \frac{EIy''(0,t)}{N} = \frac{EI}{N}\left(\frac{6}{L^2}v_2 - \frac{2}{L}\theta_2\right) \tag{3.27}$$

where M_o is the moment on the hub caused by the flexible body referred to the motor side of the system. The static friction component of T_f must now oppose both τ_a and M_o, when the speed is below the static friction threshold.

Combining the flexible and rigid bodies gives the dynamic equation:

$$M_T\begin{bmatrix}\ddot{\theta}_m \\ \ddot{v}_2 \\ \ddot{\theta}_2\end{bmatrix} + B_T\begin{bmatrix}\dot{\theta}_m \\ \dot{v}_2 \\ \dot{\theta}_2\end{bmatrix} + K_T\begin{bmatrix}\theta_m \\ v_2 \\ \theta_2\end{bmatrix} = Q\tau$$

where

$$M_T = \left[\begin{array}{cc:c} 0 & 0 & J \\ \hdashline M_B & & -F_m \\ & & -M_m \end{array}\right] \quad B_T = \begin{bmatrix} 0 & 0 & b \\ 0 & 0 & 0 \\ 0 & 0 & 0 \end{bmatrix} \quad K_T = \left[\begin{array}{cc:c} -\frac{6EI}{NL} & \frac{2EI}{N} & 0 \\ \hdashline & K_B & \begin{matrix}0\\0\end{matrix} \end{array}\right] \quad Q = \begin{bmatrix} 1 \\ 0 \\ 0 \end{bmatrix}$$

$$M_B = \frac{mL}{420}\begin{bmatrix} 156 & -22L \\ -22L & 4L^2 \end{bmatrix} \qquad K_B = \frac{EI}{L^3}\begin{bmatrix} 12 & -6L \\ -6L & 4L^2 \end{bmatrix}$$

$$\begin{aligned} \dot{x} &= Ax + Bu \\ y &= Cx \end{aligned} \tag{3.28}$$

$$\text{where } x = \begin{bmatrix} \theta_m \\ v_2 \\ \theta_2 \\ \dot{\theta}_m \\ \dot{v}_2 \\ \dot{\theta}_{2m} \end{bmatrix}, \quad y = \begin{bmatrix} \theta_a \\ v_2 \\ \theta_2 \\ \dot{\theta}_m \\ \dot{v}_2 \\ \dot{\theta}_{2m} \end{bmatrix} \text{ and } u = \tau = \tau_a - T_f. \tag{3.29}$$

$$T_f = T_{mf}\,\mathrm{sgn}(\dot{\theta}_m) + \frac{1}{N} T_{af}\,\mathrm{sgn}(\dot{\theta}_m)$$

$$A = \left[\begin{array}{c:c} 0 & I \\ \hdashline M_T^{-1}K_T & M_T^{-1}B_T \end{array}\right] \tag{3.30}$$

$$B = \left[\begin{array}{c} 0 \\ \hdashline M_T^{-1}Q \end{array}\right], \text{ and } C = \begin{bmatrix} 1/N & 0 & 0 & 0 & 0 & 0 \\ 0 & 1 & 0 & 0 & 0 & 0 \\ 0 & 0 & 1 & 0 & 0 & 0 \\ 0 & 0 & 0 & 1 & 0 & 0 \\ 0 & 0 & 0 & 0 & 1 & 0 \\ 0 & 0 & 0 & 0 & 0 & 1 \end{bmatrix}. \tag{3.31}$$

Similar to Section 3.1, if a tip mass is included in the calculations, only the mass matrix, M_B of the flexible body equations changes such that:

$$M_{BPayload} = M_{BNo\_mass} + \begin{bmatrix} m_3 & 0 \\ 0 & 0 \end{bmatrix}. \tag{3.32}$$

The rigid body equations change as described in section 2.1.

3.3 Strain Gage Reading Estimation

The second strain gage mounted on the flexible arm gives a measure of the deflection of the beam referenced to the hub. This strain gage reading can be estimated from the simulated system. The strain on the beam is proportional to the moment on the beam [16]. Therefore, the second strain gage reading is proportional to the moment on the beam at $x = 0.55$m where the second strain gage is located on the experimental apparatus.

The moment on the beam for the clamped beam is:

$$M(x) = EIy''(x,t) = EI\left(v_2\left(\frac{6}{L^2} - \frac{12x}{L^3}\right) + \theta_2\left(\frac{-2}{L} + \frac{6x}{L^2}\right)\right)$$

Therefore, for the clamped model the second strain gage reading can be approximated as:

$$SG = K_{SG}M(0.55) = K_{SG}EIy''(0.55,t) = K_{SG}EI(0.6v_2 + 1.3\theta_2),$$

where K_{SG} is a gain introduced by the strain gage circuitry.

In the clamped model v_2 and θ_2 are referenced to the hub, but in the pinned system model they are not, so the strain gage reading for the pinned mode must be approximated by:

$$SG = K_{SG}M(0.55) = K_{SG}EIy''(0.55,t) = K_{SG}EI(0.6(v_2 - \theta_a L) + 1.3(\theta_2 - \theta_a))$$

By measuring tip deflection and slope for a known strain gage reading K_{SG} is calculated as 2.27.

3.4 Experimental and Simulated Results

The system is simulated with the same constants used in Section 2.3 and with $E = 68.944$ GPa, $I = 1.1475\text{e-}10$ m^4, $m = 0.42381$ kg/m. The system is simulated with a step size of 1e-9, using C code, on an SGI Origin 2000 (Cray) and takes approximately twelve hours to run. This long simulation time is due to the small sampling time and the fact that no parallel processing was used.

The systems models are developed for both the pinned and clamped cases separately, and then the models are combined to make one model where the boundary conditions and

friction decide what state the model is in. Results are shown for an input current pulse of 3A, from 0.5 to 1 seconds. At low speeds friction affects system behaviour. Therefore, a large current input was chosen to rotate the arm through a large slew at high speeds, allowing a range of system behaviour to be seen.

Figure 3.5 and Figure 3.6 show the results for a pinned system with Coulomb friction only. No static friction has been included, since that would theoretically force the system into the clamped mode. Notice that when the speed approaches zero, the Coulomb friction causes the frequency of vibration of the system to approach the clamped frequency. The hub can still rotate and does (however slightly) in this mode as the speed is not yet zero, and therefore, the system is still pinned. The Coulomb friction, which opposes direction of motion, has a greater effect on system behaviour in this region since as the speed approaches zero it tends to oscillate about zero. Previous studies have mentioned that large hub inertias will cause the pinned frequency of vibration to approach the clamped frequency but this work is the first to note that friction at low speeds will cause the same effect on a system with small hub inertia.

Figure 3.5 shows the system simulation results using the system parameters from Table 2.1 in Chapter 2. The frequencies of vibration for the experimental and simulated case are not an exact match. However, as shown in Figure 3.6, if J_m is adjusted by 0.0003 kgm^2 the frequencies are a better match. This 12% change introduced in the inertia is within the possible experimental error.

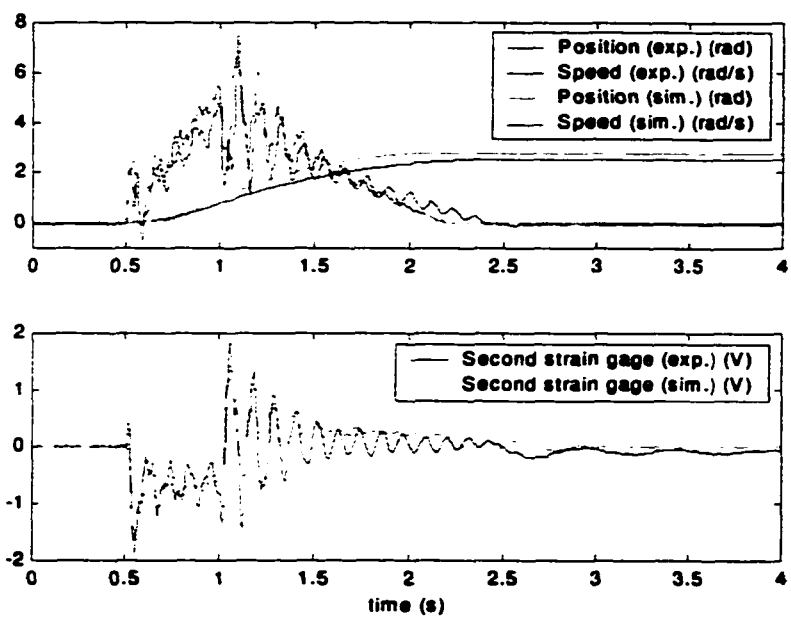

Figure 3.5 Experimental and Pinned-Mode Simulation Results using initial calculated value of J_m

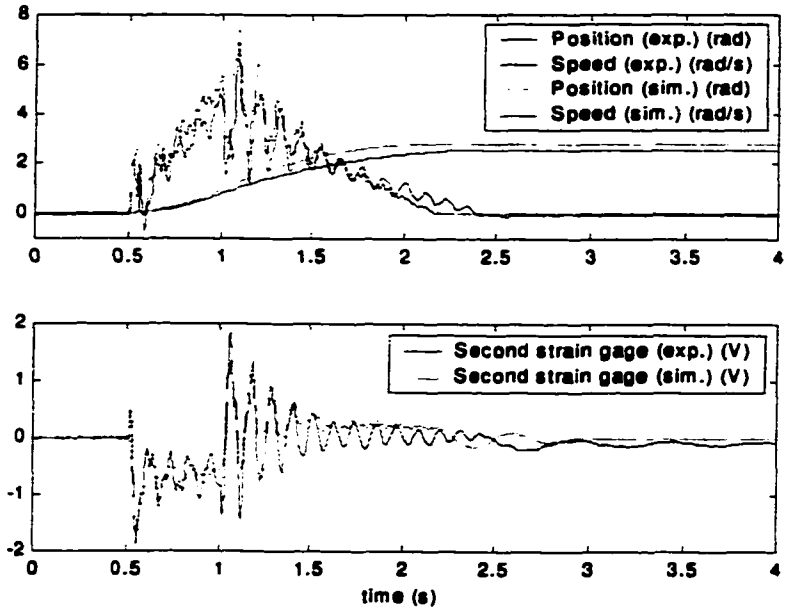

Figure 3.6 Experimental and Pinned-Mode Simulation Results using adjusted value of J_m

Figure 3.7 shows the results for the clamped model to the 3A current pulse input. The clamped system does not exhibit the right frequencies or amplitudes. This reinforces that the pinned system model must be used when the speed is not zero and the clamped model must be used when the speed is zero.

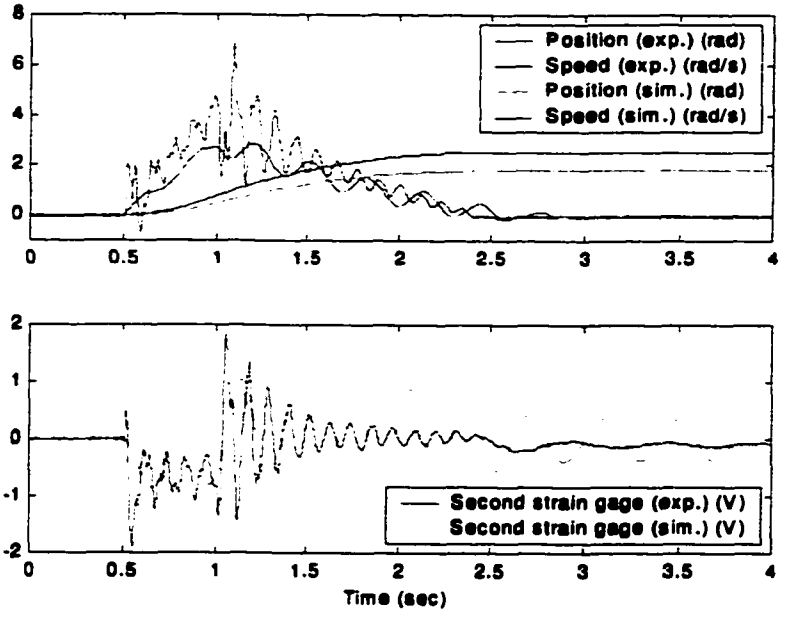

Figure 3.7 Comparison of Experimental System and Clamped-Mode Simulation

To accurately model the physical system, the two models must be combined. The simulated system switches between pinned or clamped mode based on the boundary conditions caused by friction. When the speed has remained significantly small for a period of time, static friction opposes all forces at the hub and the hub will no longer rotate. When the hub is not capable of movement the boundary conditions change and the system switches into clamped mode. Figure 3.8 compares the simulated results for the combined system with the experimental results.

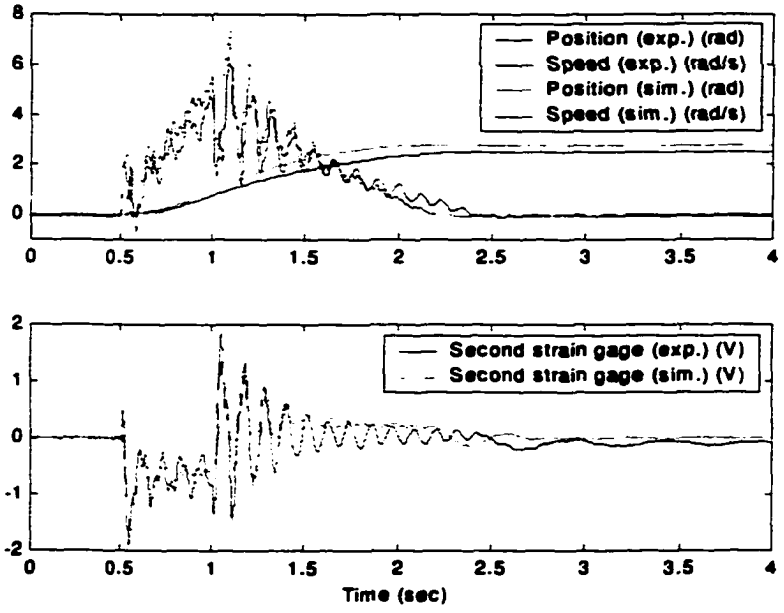

Figure 3.8 Comparison of combined system simulation and experimental results.

Figure 3.9 shows that the smooth oscillations in the physical system can be seen in the simulations if some beam damping is added to the pinned model. This also results in greater amplitude of vibration, which is closer to the experimental results. However, although there is a physical basis for determining this beam damping, the values of b and T_{sf} in Table 2.1 would need to be changed to compensate. Therefore, this damping has not been included in this model. However, the effect on the simulation of adding damping of 0.003 Nms to the pinned beam model is shown in Figure 3.9 for interest.

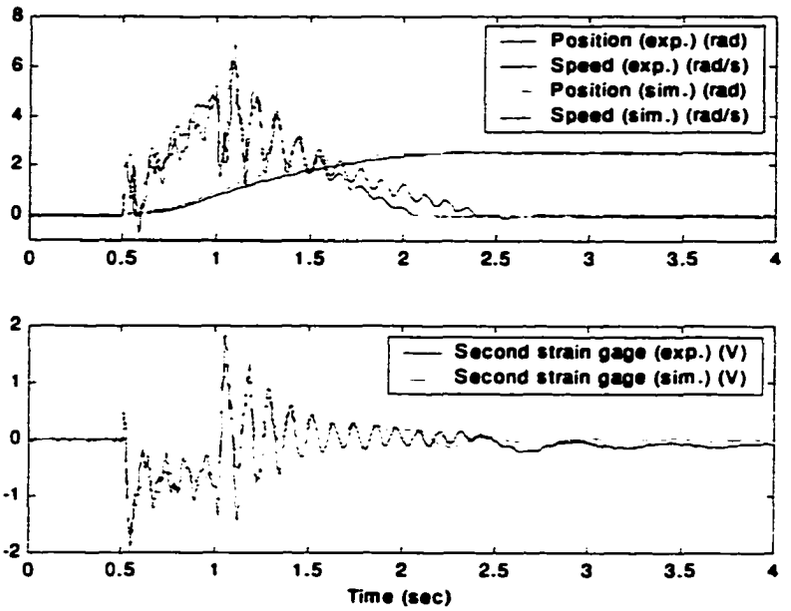

Figure 3.9 Effect on the combined system simulation caused by adding beam damping to the pinned model

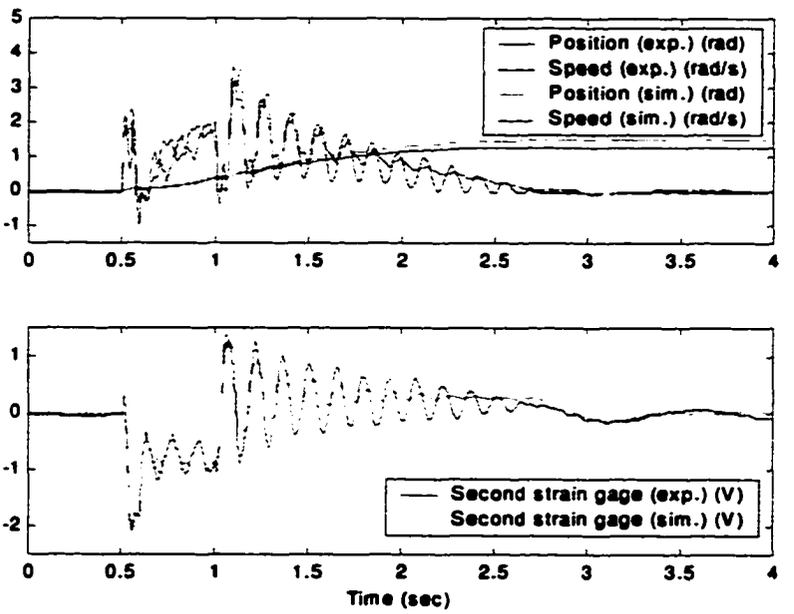

Figure 3.10 Experimental and simulation results for a payload of 300g.

Figure 3.10 shows the results of adding a 300g payload at the end of the beam. Both simulated and experimental systems show a decrease in the frequency of oscillation and increase in the amplitude of the oscillations, which take longer to decay. The advantage of modeling the flexible beam using the finite element method is that when the payload changes only the value of m_3 must be changed. With the classical methods used in [9] the

system equations must be recalculated based on the new boundary condition imposed by the payload.

3.5 Conclusions

The combined flexible/rigid body model predicts the system behaviour more accurately than the rigid body model alone. The rigid body model of Chapter 2 fails to simulate the oscillations in the motor speed, which are due to beam flexing. The flexible body model must be based on the boundary conditions of the system. While the literature suggests that either a clamped-free or pinned-free beam model can be used, this thesis shows that a system with low hub inertia exhibits both pinned and clamped behaviour due to the friction at the hub therefore the flexible body model must be able to switch between these two models based on the hub speed. When the hub speed is not zero a pinned model must be used, and when the hub speed is zero, due to static friction, a clamped model must be used. For the experimental systems modeled in previous studies [6,7,17] a clamped-free beam model was sufficient since the systems were characterized by high hub inertia or high gear ratio.

Literature has shown that high hub inertia or large gear ratio can cause the pinned mode to asymptotically approach the clamped mode. However, this thesis shows that friction at the hub can cause the pinned frequency of vibration to approach that of the clamped mode at low speeds. In this region the hub is still able to rotate, however, and therefore the pinned model must be used. When the hub can no longer rotate due to static friction effects a clamped model must be used.

The finite element model allows for the inclusion of payload mass as a variable without the need to recalculate the system equations if the payload changes.

Experimental results indicate that hub speed is affected by the flexing of the arm since vibrations in the hub speed are delayed versions of the vibrations indicated by strain gage readings. Although the clamped model is only appropriate when hub motion is prevented by static friction, the clamped model includes a reaction term for the torque on the hub due to beam flexing. This reaction torque can be predicted by the strain gage readings which indicates that strain feedback would be useful in eliminating vibration. Since the pinned model has no explicit reaction term Chapter 4 studies the effect, on the flexible arm vibrations, of adding the clamped model reaction torque to the control effort.

Chapter 4

Controller Design

The model developed in Chapter 3 is a combination of two separate models that depend on the boundary conditions: a pinned model, and a clamped model. However in terms of behaviour the system can be divided into three separate regions: pinned system under high-speed conditions, pinned system under low-speed conditions, and clamped system. Under low-speed conditions the friction in the system changes the pinned system behaviour, yet the arm can still rotate. When the forces at the hub are no longer able to overcome the friction forces, the system becomes clamped. By simulating the system with different vibration-suppressing controllers it can be shown that the system responds differently to each controller depending on what region it is in.

It has been shown in [11,22,23] that tip acceleration feedback assists in vibration suppression. Strain gage feedback is used in [21] to reduce flexible arm vibration. Previous works have mentioned the intuitive appeal of using tip acceleration or strain gage feedback for vibration suppression. This thesis uses the strain gage to approximate the coupling torque used in the clamped model developed in Chapter 3. The coupling torque is used to combine the rigid and flexible body equations and suggests that applying a controller to oppose this coupling torque will reduce vibrations at the hub.

Although there are many complex controllers that could be applied to the system model, the vibration-suppressing controller considered here uses signals available for feedback from the experimental system, avoiding the need for an observer, and can be intuitively tuned.

Vibration-suppressing controllers, based on the coupling torque described in Chapter 3, are considered for the two separate models in the three distinct regions of behaviour, and then for the complete system model. These are discussed in Sections 4.1 – 4.4. In demonstrating the vibration-suppressing controllers no setpoint is used. A current pulse of 3A and 0.5 second duration is applied to the motor with the vibration-suppressing controller added directly to this, as in Equation (4.1), as opposed to the traditional negative feedback arrangement, so that the effect of the vibration-suppressing controller on system behaviour may be observed.

$$i_a = \begin{cases} 3 + \dfrac{K_{mo}(M_o(t-t_d))}{k\phi} & \text{A for } 0 \le t \le 0.5\,\text{s} \\ \dfrac{K_{mo}(M_o(t-t_d))}{k\phi} & \text{A for } t > 0.5\,\text{s} \end{cases} \tag{4.1}$$

The controller is then combined with PD control, based on rigid body hub measurements. In Section 4.5 a comparison is made to PD control alone in response to a setpoint of 100 degrees.

The results of the experimental system using vibration-suppressing controllers and PD control are also shown. For the experimental system the control is implemented as shown in Figure 4.1, where the second strain gage is used as an approximation to M_o. In the simulations the calculated value of M_o is used.

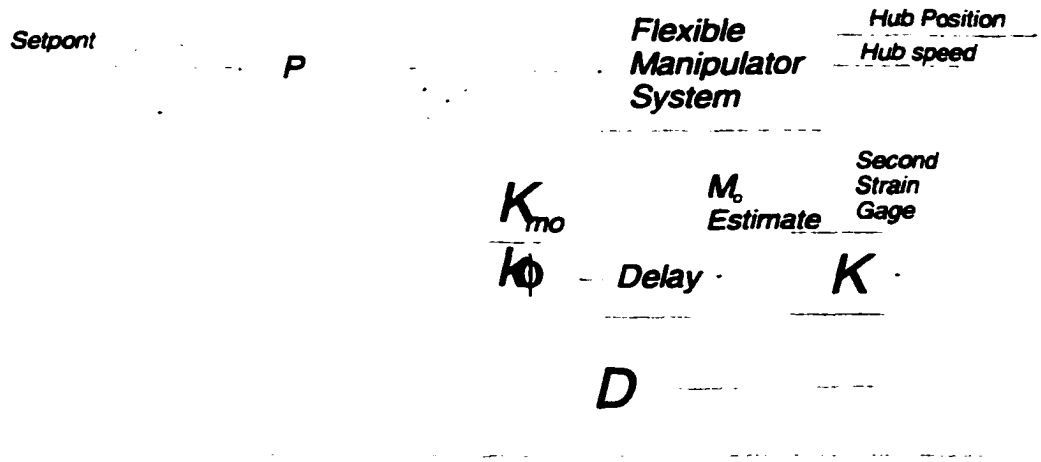

Figure 4.1 Block diagram of PD plus vibration suppression control.

$$i_a = K_p error - K_d(hub\ speed) + \frac{K_{mo}(M_o(t-t_d))}{k\phi} \tag{4.2}$$

4.1 Controller Design Based on Clamped Model

In the clamped system model developed in Chapter 3, the flexible body is coupled to the rigid body through M_o, given in Equation (3.27), which is repeated here.

$$M_o = M(0) = \frac{EI}{N}\left(\frac{6}{L^2}v_2 - \frac{2}{L}\theta_2\right). \tag{4.3}$$

By applying a control effort opposing M_o, it is expected that the effect of the flexible

body on the rigid body can be eliminated. The response of the clamped system model (without friction) to the control effort of Equation (4.1), with $K_{mo} = -1$ and $t_d = 0$, is shown in Figure 4.2. Although, the vibration of the beam is no longer reflected in the speed, the vibration of the beam is not reduced. For the clamped system, a control effort of Equation (4.1), with $K_{mo} = -1$, and $t_d = 0.074$ seconds which is the time delay between the oscillations in the second strain gage reading and the hub speed (based on the uncontrolled system model in Figure 3.7), gives a good reduction in beam vibration, as shown in Figure 4.3. The clamped model shows a mutual interaction between speed and the strain gage reading since feeding back strain gage vibrations eliminates vibrations in speed, and feeding back vibrations in speed eliminates vibrations in strain.

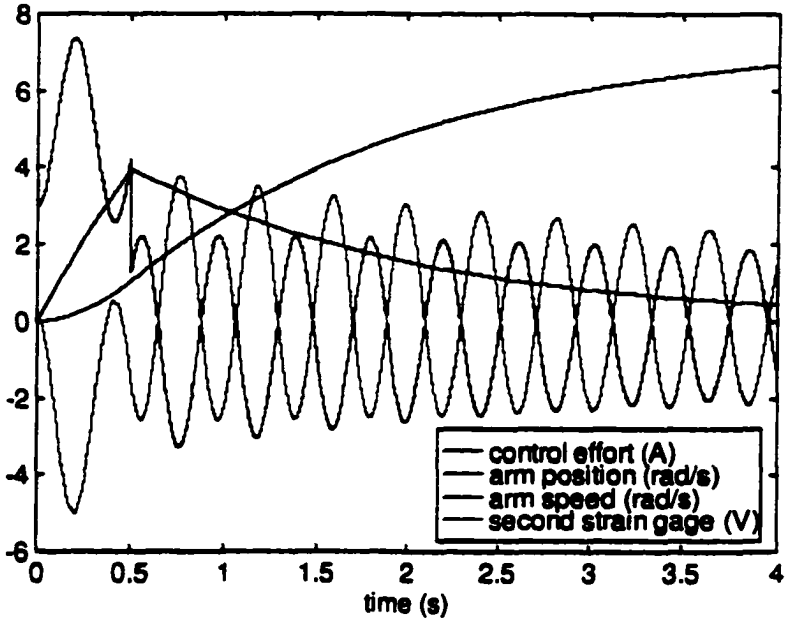

Figure 4.2 The clamped system model response for $K_{mo} = -1$ and $t_d = 0$.

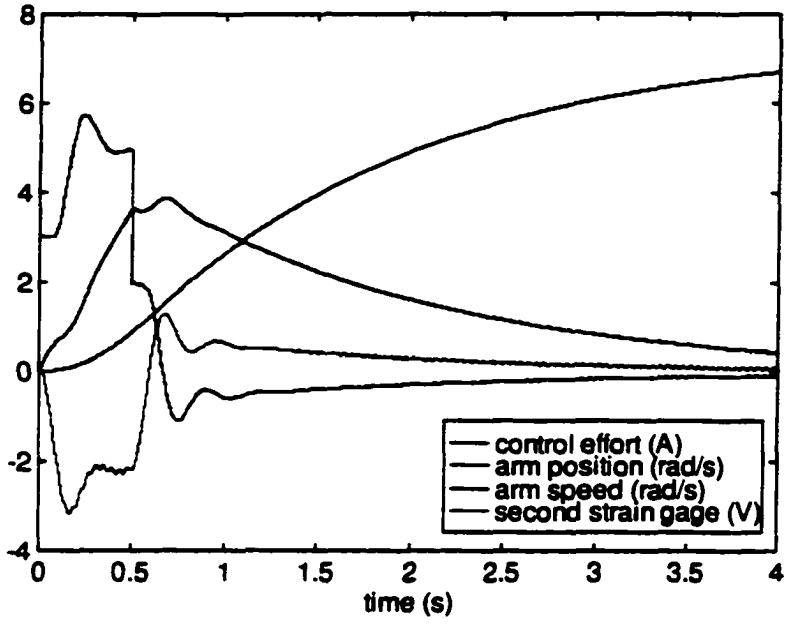

Figure 4.3 The clamped system model response for K_{mo} = -1 and t_d = 0.074 sec.

The pinned model, which is not explicitly coupled, does not exhibit this behaviour. If a control effort of Equation (4.1), with K_{mo} = -1, and t_d = 0.026 seconds which is the time delay between the oscillations in the second strain gage reading and the hub speed (based on the uncontrolled system model in Figure 3.6), is applied to a pinned system as shown in Figure 4.4, the response is unstable. This indicates that the behaviour of the pinned and clamped models is different. Therefore, a clamped model will not accurately model a pinned system and a model should be chosen based on the system boundary conditions. Figure 4.4 and Figure 4.5 show the simulated results for the pinned system, without and with a current limit of 5A. Note that for the pinned system the reference for v_2 and θ_2 is different and M_o must be calculated using Equation (4.4).

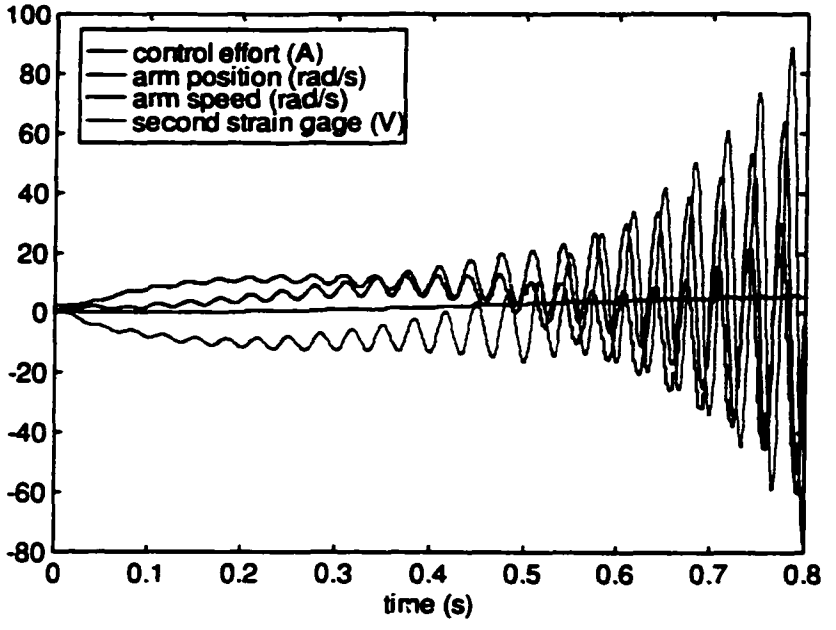

Figure 4.4 The pinned system model (with friction) response for K_{mo} = -1 and t_d = 0.026 sec.

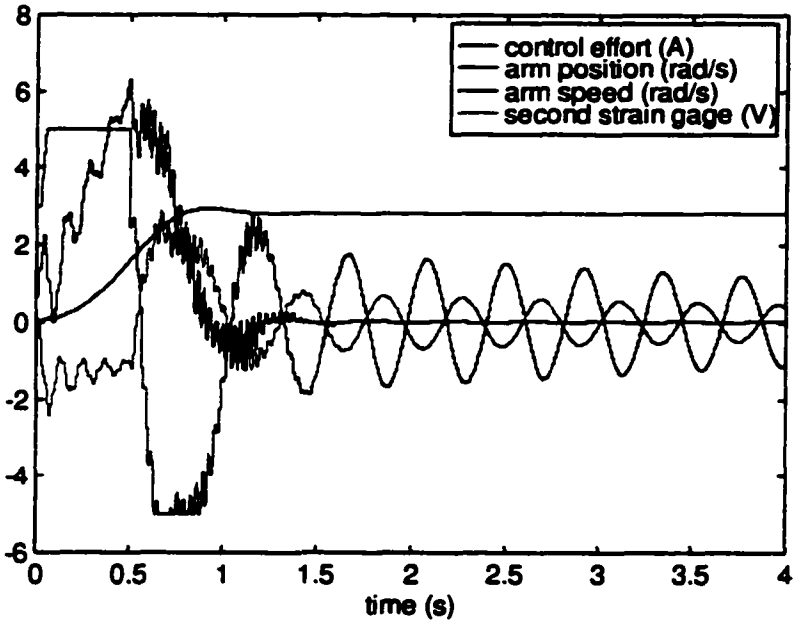

Figure 4.5 Pinned system model response, for K_{mo} = -1 and t_d = 0.026 sec., with current limited to 5A.

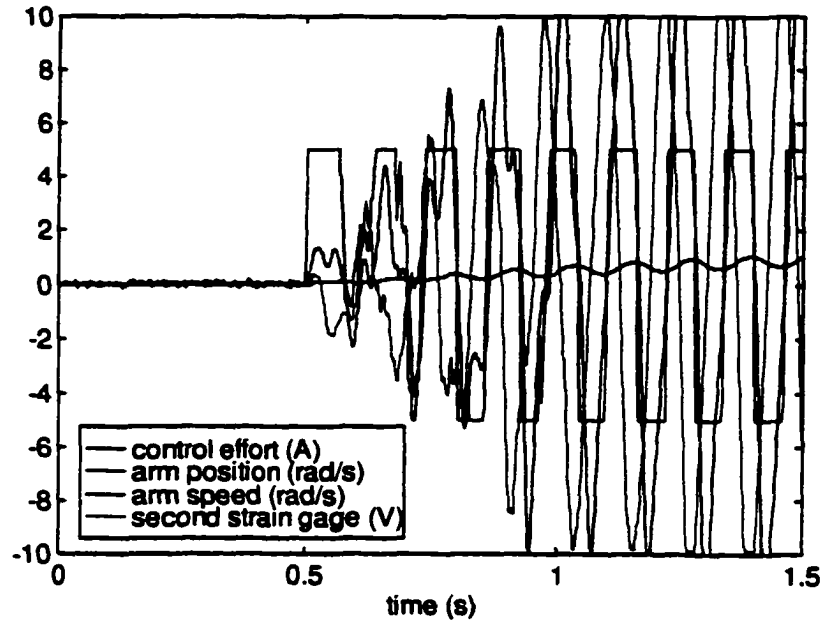

Figure 4.6 Experimental system response, for K_{mo} = -1 and t_d = 0.026 sec., with current limited to 5A.

Figure 4.6 shows the response of the experimental system. It is not surprising that the experimental system is unstable even when the current is limited to 5A, since, in Chapter 3, the experimental system showed larger oscillations in the strain gage than the simulated system for the same input and for the experimental system control the second gage reading is used to approximate M_o. When the second strain gage reading is delayed and fed back the controller quickly saturates and continues to oscillate within the saturation limits.

4.2 Controller Design Based on Pinned Model without Friction

Simulation results are shown in Figure 4.7 for the pinned model without Coulomb friction. The coupling between the rigid and flexible bodies is not via an explicit coupling term for the pinned system and a reaction torque cannot be determined for this system. However, if a control effort of Equation (4.1) is applied, with K_{mo} = -1, and t_d = 0 seconds, and with M_o calculated using Equation (4.4), a reduction of beam vibration is observed. M_o must be calculated using Equation (4.4) since in the pinned model v_2 and θ_2 are not referenced to the hub.

$$Mo = \frac{6EI}{L^2 N} EI(v_2 - \theta_a L) - \frac{2}{LN} EI(\theta_2 - \theta_a). \tag{4.4}$$

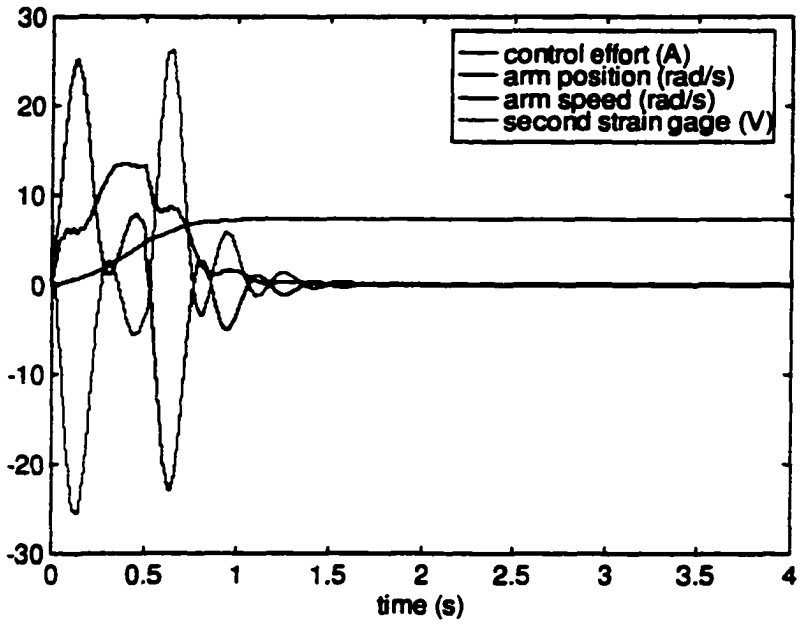

Figure 4.7 The pinned system model response, for K_{mo} = -1 and t_d = 0 sec.

4.3 Controller for Pinned Model with Friction

In the pinned system with friction, when Coulomb friction affects the beam behaviour at low speeds, the controller of Section 4.2, which has K_{mo} = -1 and t_d = 0 sec, does not effectively reduce beam vibration, even when friction compensation is applied as shown in Figure 4.8 and Figure 4.9. The friction compensation is applied at low speeds only by opposing the Coulomb friction in the system (values shown in Table 2.1) in both magnitude and direction. Based on the experimental results of Figure 3.1 motor speed less than 0.03 rad/s (where the frequency of oscillation changes) is considered to be low speed.

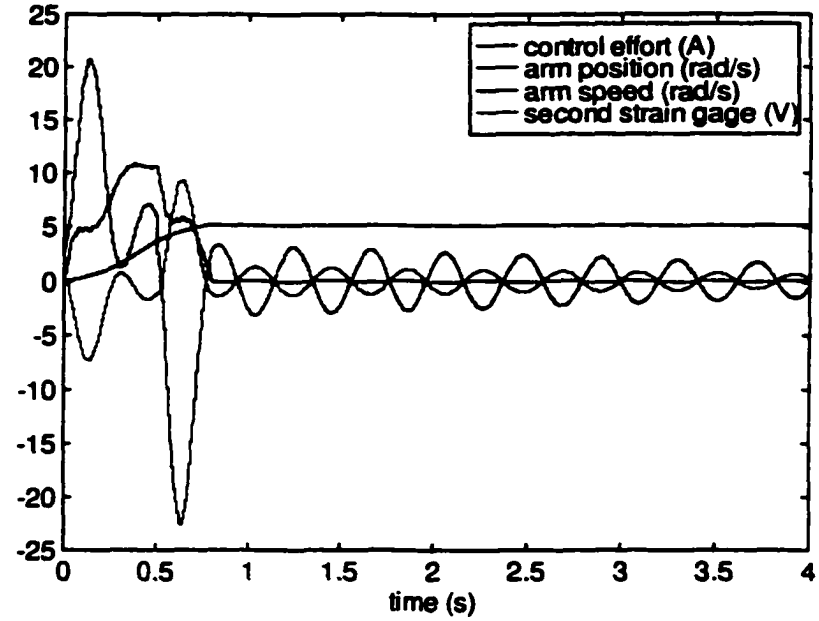

Figure 4.8 The pinned system model (with friction) response, for K_{mo} = -1 and t_d = 0 sec.

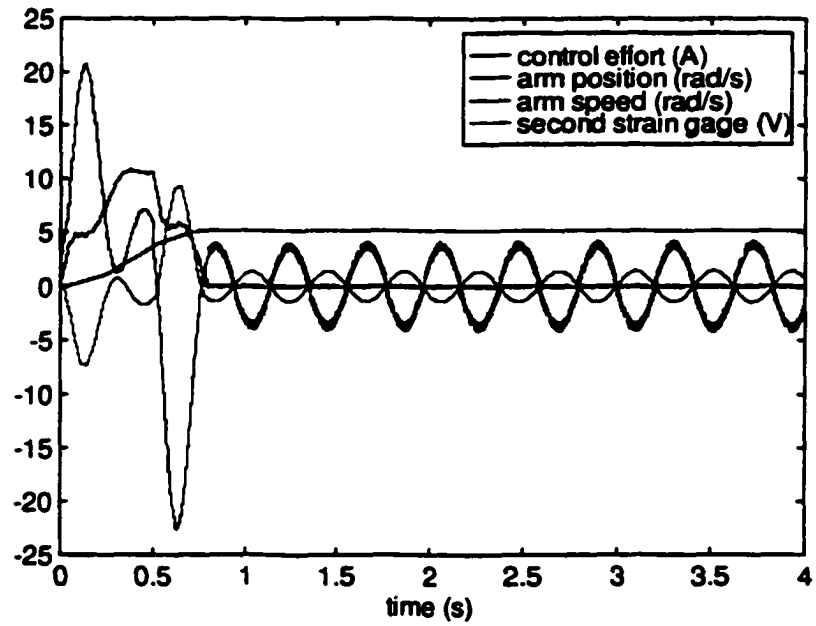

Figure 4.9 The pinned system model (with friction) response, for K_{mo} = -1 and t_d = 0 sec. plus low-speed friction compensation.

The vibration-suppressing controller that is effective in the low-speed region is the controller of Equation (4.1), with K_{mo} = 1 and t_d = 0, plus friction compensation. Figure 4.10 shows this controller without friction compensation. The controller actually increases the vibrations of the system until the speed is small where it is effective in suppressing them. Adding friction compensation in the low-speed region makes the

controller more effective in dampening vibration as shown in Figure 4.11.

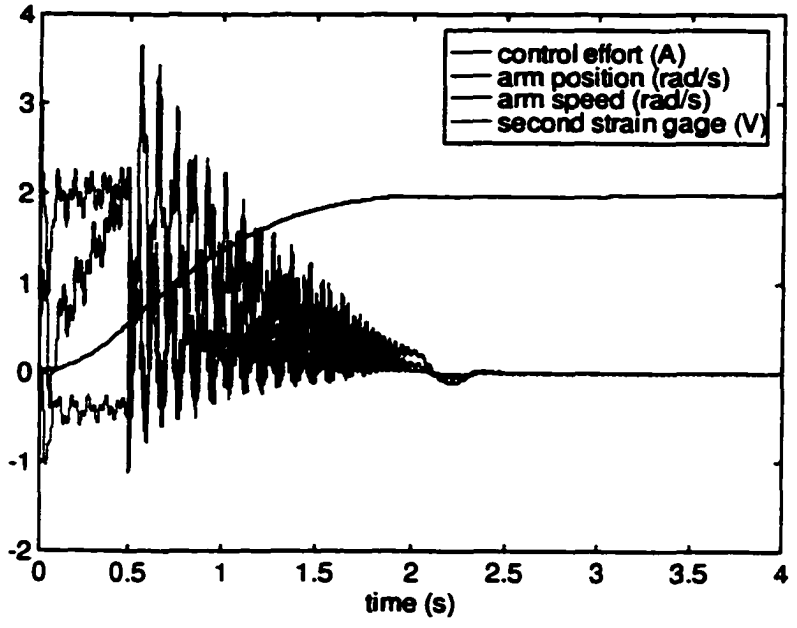

Figure 4.10 The pinned system model (with friction) response, for K_{mo} = 1 and t_d = 0 sec.

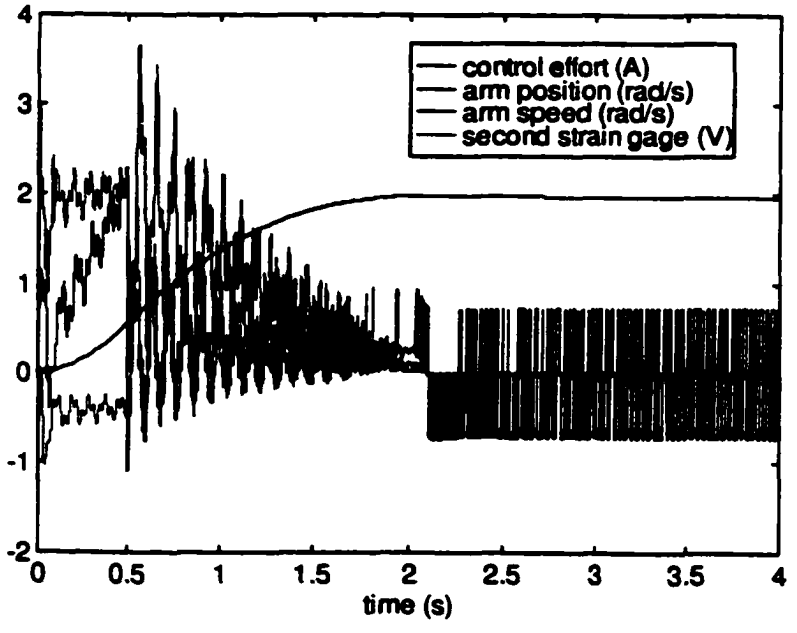

Figure 4.11 The pinned system model (with friction) response, for K_{mo} = 1 and t_d = 0 sec, plus low-speed friction compensation.

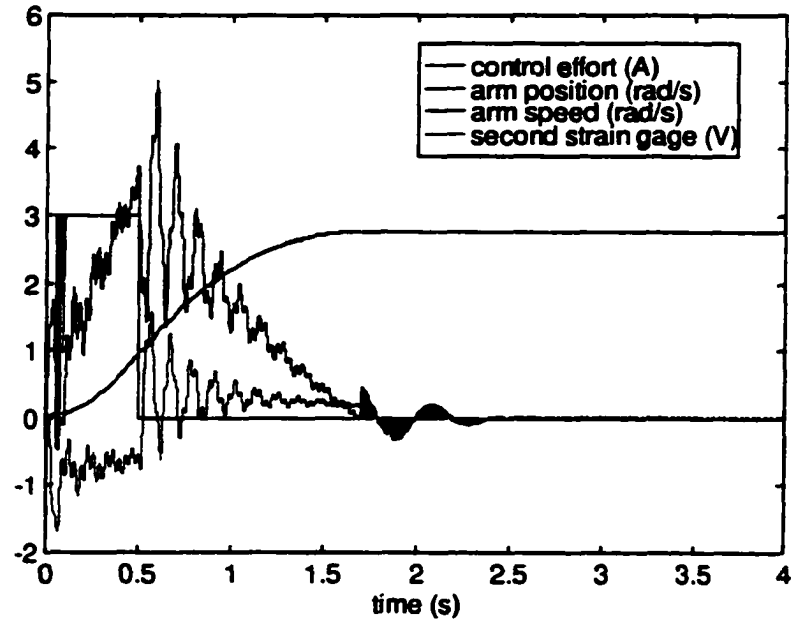

Figure 4.12 The pinned system model (with friction) response, for K_{mo} = -1 and t_d = 0 sec., with the controller applied at low speed only.

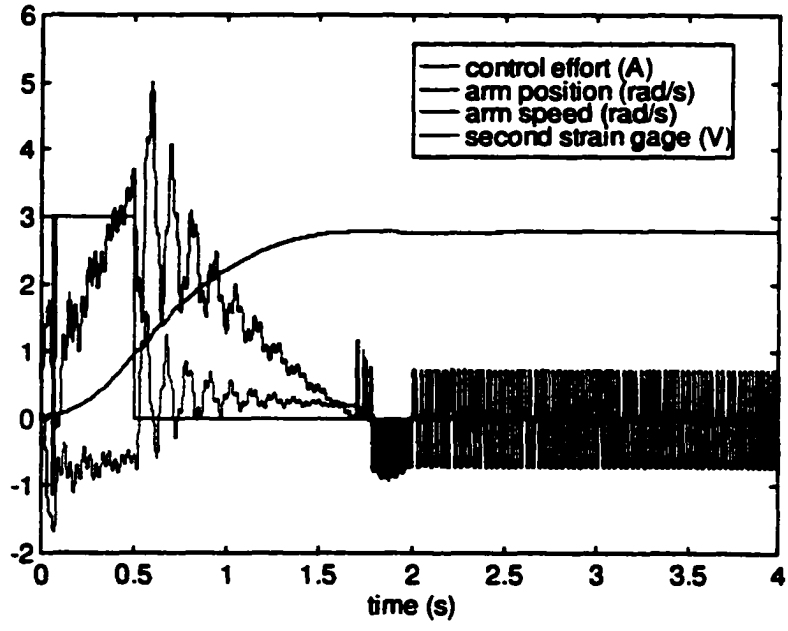

Figure 4.13 The pinned system model (with friction) response, for K_{mo} = -1 and t_d = 0 sec., with the controller applied at low speed only plus low-speed friction compensation.

Figure 4.12 and Figure 4.13 show that applying the vibration-suppressing controller only at low speeds effectively damps vibrations of the beam (by the time the hub has reached steady-state) without affecting system behaviour at high speeds.

4.4 Vibration-suppressing Controller Design for the Complete System

Since the system responds differently to controllers in the pinned, high-speed region (hub speed equal to or greater than 0.03 rad/s), the pinned, low-speed region (hub speed less than 0.03 rad/s) and the clamped region (hub speed equal to zero), the system needs a vibration-suppressing controller that changes depending on the region. The best controller for the pinned region of system at high speeds is the controller of Equation (4.1) with $K_{mo} = -1$ and $t_d = 0$. For the pinned region of the system at low speeds the best controller has $K_{mo} = 1$ and $t_d = 0$ with additional friction compensation. A controller will not be effective in the clamped mode since any control applied in this region will either have no effect (if it is less than the friction level) or it will force the system into pinned mode where a pinned mode controller would function more effectively. Therefore no controller is suggested for the clamped region. Instead, control should be applied in such a way that when the static friction finally prevents the hub from moving the flexible arm vibrations are already significantly reduced and further control is unnecessary.

Figure 4.14 shows the simulation results for this combined controller. The controller was not constrained to show the system response for the ideal situation of unlimited control effort.

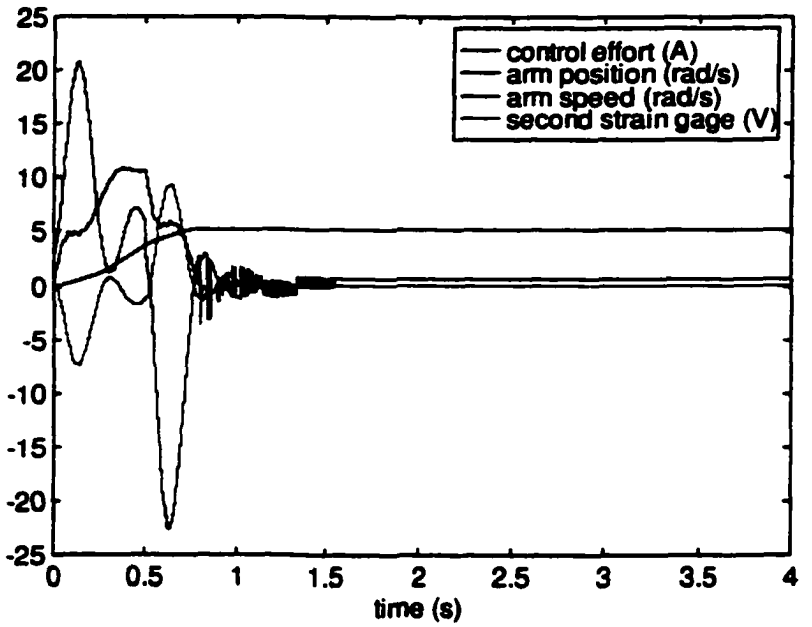

Figure 4.14 Complete system model with a combined controller.

4.5 System Response to PD Control with Added Vibration-suppressing Control

It now remains to be seen if this combined vibration-suppressing controller can be an

effective addition to a proportional plus velocity feedback controller (PD controller). Figure 4.16 shows the system response for a setpoint of a 100-degree slew and a controller with PD gains used in Chapter 2 (P=2.5308, D=0.6625) combined with the vibration-suppressing controller while Figure 4.15 shows the response for PD control alone.

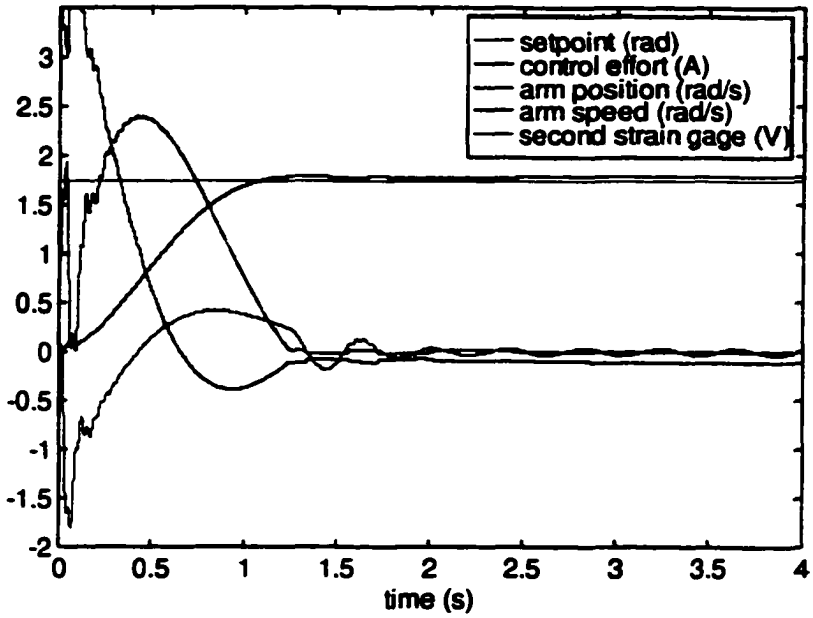

Figure 4.15 System response to a setpoint of 100° with PD control.

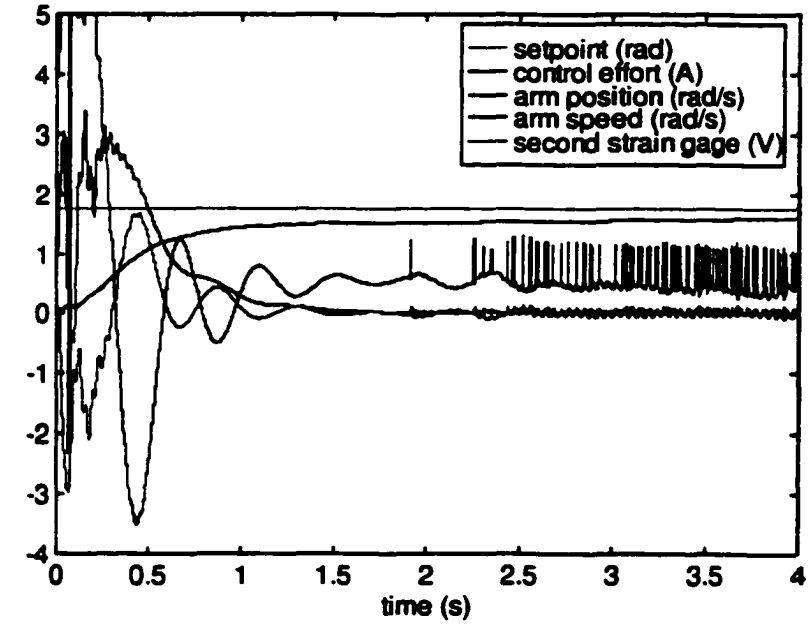

Figure 4.16 System response with PD and combined controller.

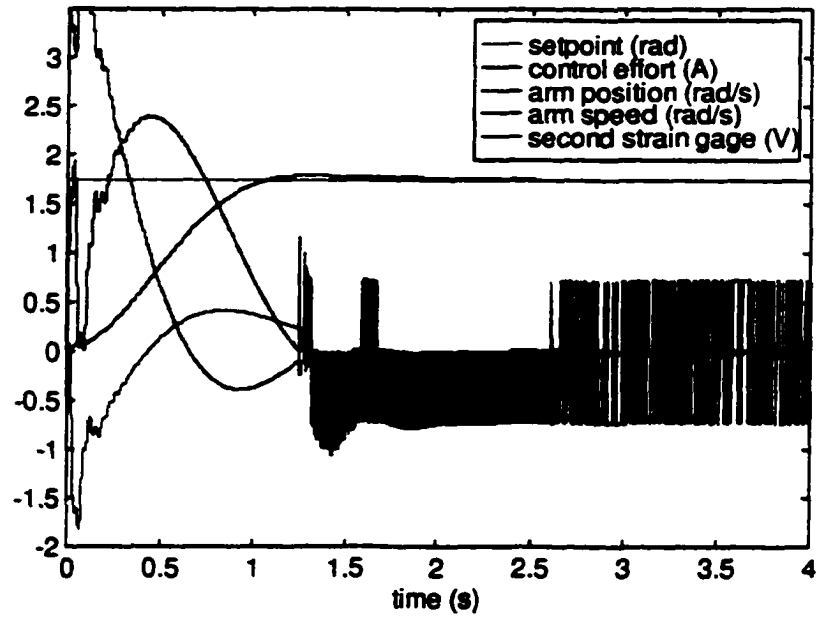

Figure 4.17 Total system with PD control and with vibration-suppressing control in the low-speed pinned region and clamped region only.

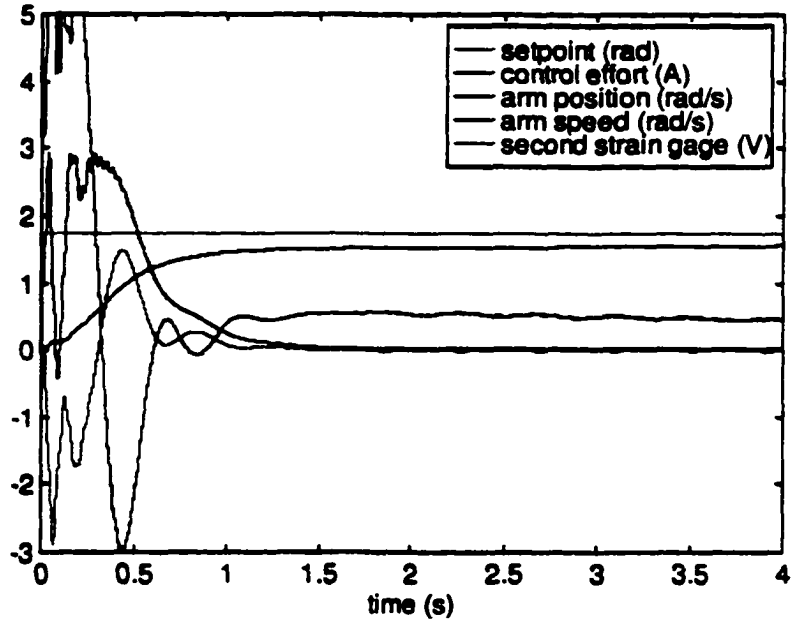

Figure 4.18 Total System with PD Control and with vibration-suppressing control at high speeds only.

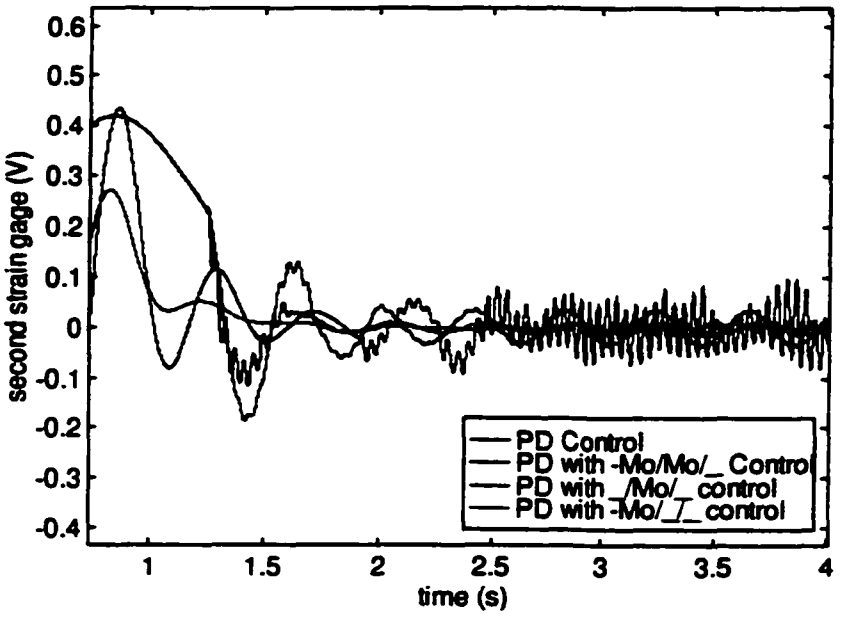

Figure 4.19 Strain Gage Comparisons.

A comparison of Figure 4.15 and Figure 4.16 shows that an increase in steady-state hub position error is observed in Figure 4.16. However, by the time the hub position has reached steady-state, the flexible arm vibrations are reduced as compared to Figure 4.15. The system response to PD control with vibration-suppressing control (as per Section 4.4) in the low-speed pinned and clamped regions only is shown in Figure 4.17. From comparison of Figure 4.15, Figure 4.16 and Figure 4.17, the best results are achieved for vibration suppression control in the low-speed pinned and clamped regions only, added to the PD control. Steady-state hub position error is the same as for PD control alone however flexible arm vibrations at the time the hub speed goes to zero are reduced. Unfortunately, as shown in Figure 4.16, Figure 4.17 and Figure 4.19, when friction compensation is applied at low speeds the system tends to overcompensate. In a system with noise, this effect is amplified and the overall response is poor. Therefore the most practical controller for suppressing vibration is the vibration-suppressing controller for the high-speed pinned region only (with no vibration-suppressing controller at low speeds), as shown in Figure 4.18, which reduces the oscillations, as much as possible, before static friction prevents the hub rotation.

The experimental results for this controller are shown in Figure 4.21, while Figure 4.20 shows the experimental results for PD control only. The experimental second strain gage reading is used to approximate M_o by multiplying the reading by a gain, K, as shown in Figure 4.1. Based on comparison of experimental data with simulated data a gain of K = 1.18 was used. The vibration of the flexible arm when the hub position has reached steady-state is reduced as shown in Figure 4.21, however there is an increase in steady-state hub position error. Figure 4.22 compares the strain gage readings of Figure 4.20 and Figure 4.21. Additionally, for the experimental system, it is difficult to separate the low-speed pinned region (where the hub can still rotate) from the clamped region (where

static friction prevents hub rotation) due to the noisy speed signal; therefore applying the vibration-suppressing controller of Section 4.4, for the low-speed regions, would be difficult.

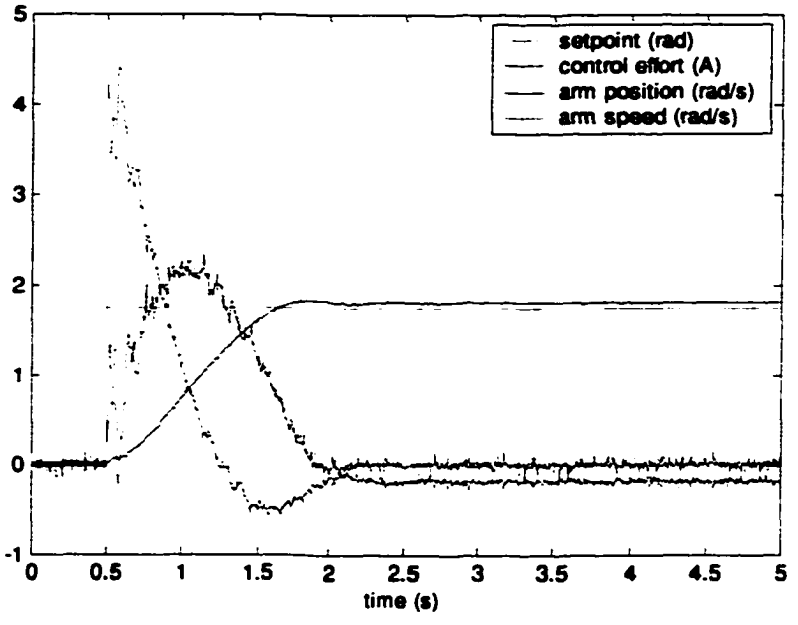

(a)

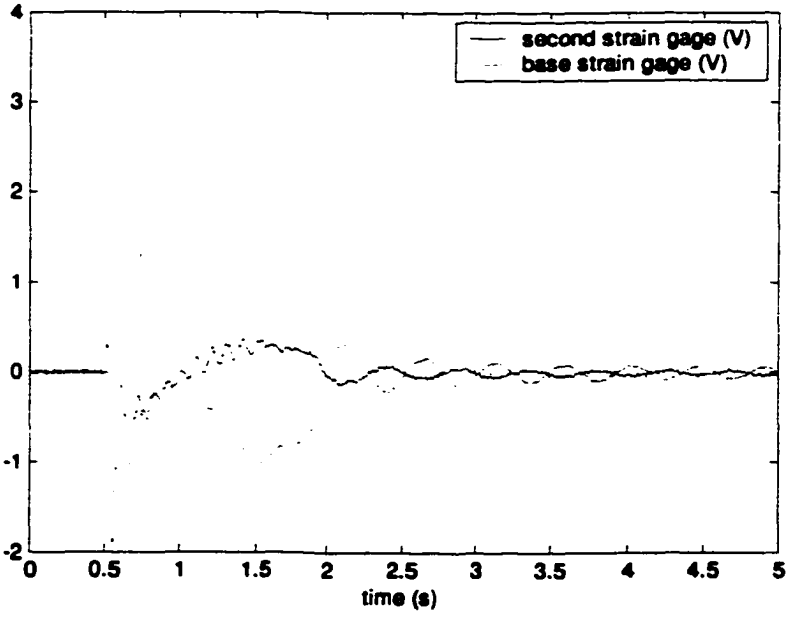

(b)

Figure 4.20 Experimental System with PD control.

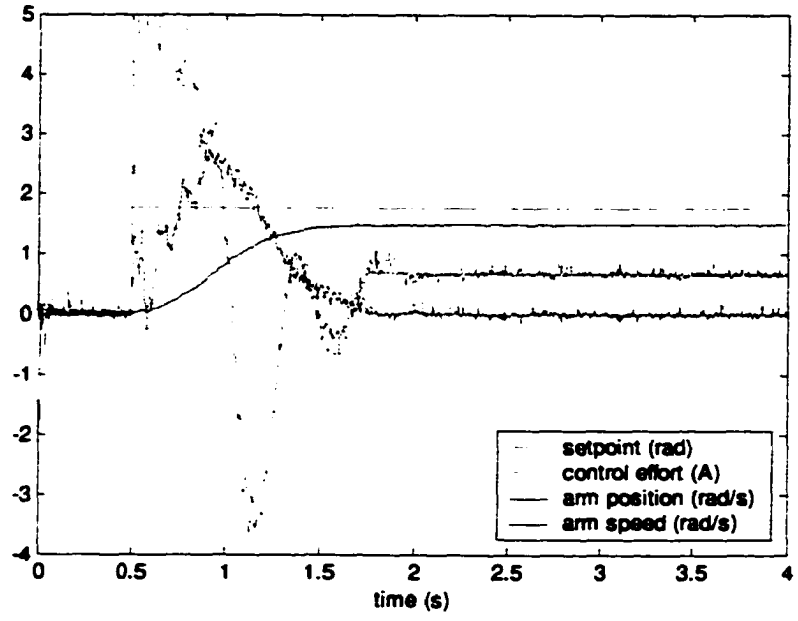

(a)

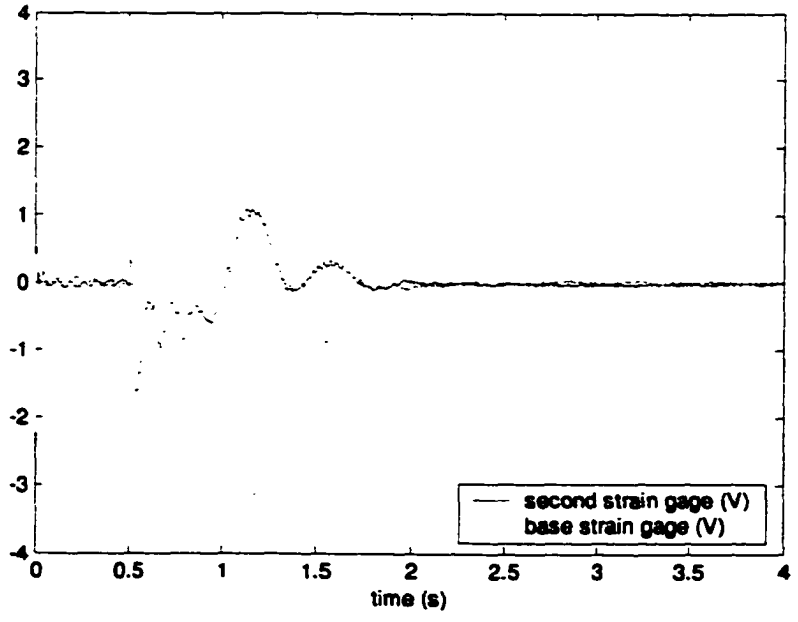

(b)

Figure 4.21 Experiment response for a PD control with vibration-suppressing control at high speed.

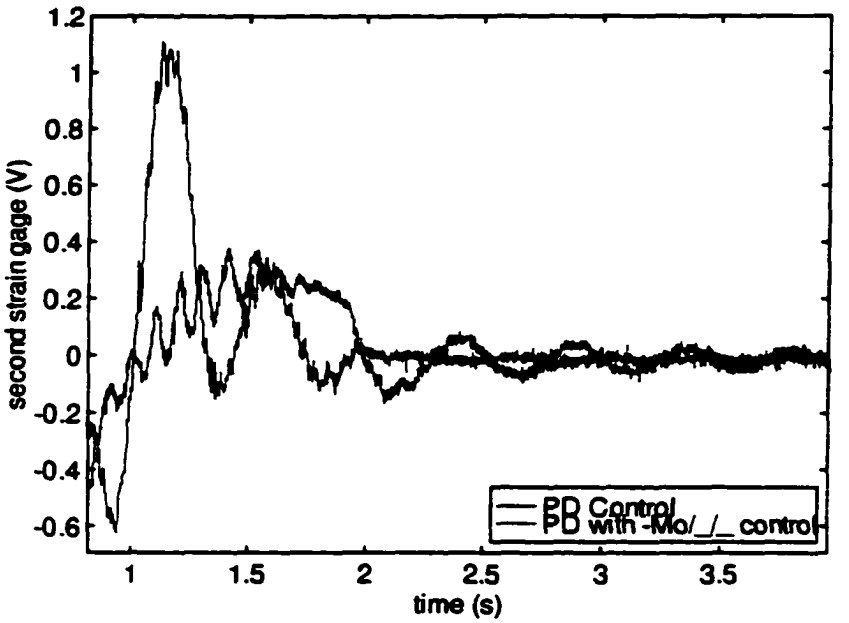

Figure 4.22 Experiment Strain Gage Comparisons.

4.6 Conclusions

The combined model has three main regions of behaviour – pinned system at high speed, pinned system at low speed and clamped system. Each region responds differently to vibration-suppressing controllers, and theoretically, for maximum effectiveness a different controller should be used in each region. Notably, the controller that effectively suppresses vibration in the clamped-system simulations, is unstable in pinned-system simulations and when applied to the experimental system. Previous studies [21] have noted that a phase shift introduced on strain feedback can make the system unstable.

Friction compensation in the low-speed pinned region tends to overcompensate. The noise in the experimental system would increase these vibrations making the vibration-suppressing control ineffective at low speeds. The most effective vibration suppression controller for the experimental system, therefore, is the vibration-suppressing controller for the high-speed pinned region only, with no vibration-suppressing controller applied at low speeds.

When added to a PD controller the vibration-suppressing controller is effective in reducing the flexible arm vibration by the time the hub position has reached steady-state at a cost of some steady-state hub position error.

The vibration suppression controller presented in this chapter is advantageous in that it uses available sensor readings and can be intuitively tuned for an experimental system without running simulations. This controller is computationally efficient and inexpensive which makes it easy to implement and maintain.

Chapter 5

Conclusions and Future Work

This thesis has produced several new observations on the behaviour of flexible manipulator systems. A flexible manipulator system with friction will exhibit both pinned and clamped frequencies of vibration. At high speeds, for a system with low hub inertia, the arm is able to rotate and exhibits pinned frequencies. When the speed is zero and static friction at the hub prevents the arm from rotating, it vibrates at clamped frequencies. Therefore, to model the complete system, a pinned and a clamped model must be used and the boundary condition at the hub must be used to switch between models.

This thesis also demonstrates that at low speeds friction causes the pinned frequencies of vibration to approach the clamped frequencies. This region differs from the clamped region since the hub is still capable of small movement. Therefore, a flexible arm system has three different regions of behaviour: pinned at high speeds, pinned at low speeds and clamped. In simulation, each of these regions responds differently to vibration-suppressing controllers, thus requiring a different controller in each region for maximum performance. Vibration suppression controllers based on feedback of a strain gage reading from the beam are demonstrated for each region through simulation. Practically, while the controller used in the high-speed region provides good vibration suppression, the best control in the low-speed region is no controller due to the noise in the strain gage reading. Experimental and simulation results demonstrate that the final vibration suppression controller design, when added to PD control, reduces arm vibration by the time the hub position reaches steady-state compared to PD control alone.

A non-linear model, which includes friction and is valid for small and large rotation angles, is used to model the system. The small amount of backlash, due to the gears in the experimental system, has little effect on system behaviour and has not been included in the final model. Payload mass can be easily added to the model without the need to recalculate the beam model equations.

Suggestions for future work:

- Investigate filtering techniques on strain gage measurements so that feedback in the pinned, low-speed region can be practically applied yet avoid introducing a phase shift which will make the system unstable.

- Investigate methods of friction compensation such that position control and vibration suppression are improved without a large increase in settling time.

- Explore controller design based on an estimation of payload mass from the fundamental frequency of the system. It has been shown in [14] that fundamental frequency estimation is possible within a quarter to half cycle of the period of the fundamental. Investigate whether the technique of [14] can be effectively applied to the flexible manipulator system. If this technique were successful it would be an improvement over the estimation times shown in [22,23].

- Placing constraints on the rate of change of motor current effectively reduced initial beam vibration as shown in Chapter 2. Further investigation is needed to determine the overall effect on system performance of constraining the rate of change of motor current when controllers other than PD controllers are applied.

- Investigate improved modeling techniques for determining strain gage dynamics based on flexible arm behaviour.

References

[1] Atherton, D.P., *Nonlinear Control Engineering*, ISBN 0-442-30486-2, Van Nostrand Reinhold Co. Ltd., 1982.

[2] Book, W. J., Maizza-Neto, O., and Whitney, D. E., Feedback Control of Two Beam, Two Joint Systems with Distributed Flexibility. *Journal of Dynamic Systems, Measurement and Control*, 1975, pp. 424-431.

[3] Cannon Jr., R. H. and Schmitz, E., Initial Experiments on the End-Point Control of a Flexible One-Link Robot. *International Journal of Robotics Research*, 1984, 3(3), pp. 62-75.

[4] Davis, J. H. and Hirschorn, R. M., Tracking Control of a Flexible Robot Link. *IEEE Transactions on Automatic Control*, 1988, 33(3), pp. 238-248.

[5] Feliu, V., Rattan, K. S., Brown Jr., H. B., Modelling and Control of Single-Link Flexible Arms with Lumped Masses. *Journal of Dynamic Systems, Measurement and Control*, 1992, **114**, pp. 59-69.

[6] Geniele, H., Patel, R. V., and Khorasani, K., Control of a Flexible-Link Manipulator. *Proceedings of 1995 IEEE International Conference on Robotics and Automation*, 1995, pp. 1217-1222.

[7] Geniele, H., Patel, R. V., and Khorasani, K., End-Point Control of a Flexible-Link Manipulator: Theory and Experiments. *IEEE Transactions on Control Systems Technology*, 1997, 5(6), pp. 556-570.

[8] Hastings, G. G. and Book, W. J., Experiments in Optimal Control of a Flexible Arm. *Proceedings of the 1985 American Control Conference*, 1985, pp. 728-729.

[9] Hastings, G. G. and Book, W. J., Verification of a Linear Dynamic Model for Flexible Robotic Manipulators. *Proceedings 1986 IEEE International Conference on Robotics and Automation*, 1986, pp. 1024-1029.

[10] Jacobsen, Lydik S., and Ayre, Robert S., *Engineering Vibrations*, McGraw-Hill Book Company, Inc., 1958.

[11] Kotnik, P. T., Yurkovich, S. and Ozguner, U., Acceleration Feedback Control of a Flexible Manipulator Arm. *Journal of Robotic Systems*, 1988, 5(3), pp. 181-196.

[12] Krishnan, H. and Vidyasagar, M., Control of Single-Link Flexible Beam Using Hankel-Norm-Based Reduced-Order Model. *IEE Proc.-Control Theory Appl.*, 1998, 145(2), pp. 151-158.

[13] Leonard, W., *Control of Electrical Drives*, Springer-Verlag, 1985.

[14] Natarajan, K., and Sivakumar, Seshadri, Design of a fixed-point digital filter for state estimation for UPS applications, *Can. J.Elect. & Comp. Eng.*, 1999, **24**(4), pp.155-161.

[15] Nelder, J. A., and Mead, R.., A Simplex Method for Function Minimization, *Computer Journal*, vol. 7, pp. 308-313, 1965.

[16] Popov, Egor P., *Introduction to mechanics of solids*, Prentice-Hall, Inc., 1968.

[17] Sakawa, S., Matsuno, F., and Fukushima, S., Modeling and Feedback Control of a Flexible Arm, *Journal of Robotic Systems*, 1985, **2**(4), pp. 453-472.

[18] Taylor, J. H. and Lu, J., Robust Nonlinear Control System Synthesis Method for Electro-Mechanical Pointing System with Flexible Modes. *Journal of Systems Engineering*, 1995, **5**, pp. 192-204.

[19] Thomson, T. and Dahleh, M.D., *Theory of Vibration with Applications*, ISBN 0-13-651068-X, Prentice-Hall, Inc., 1998.

[20] Wang, D. and Vidyasagar, M., Transfer Functions for a Single Flexible Link. *Proceedings 1989 IEEE International Conference on Robotics and Automation*, 1989, pp. 1042-1047.

[21] Yu, Sicheng, Control of a Flexible-Link Manipulator, Masters Thesis, Lakehead University. 1997.

[22] Yurkovich, S., Pacheco, F. E. and Tzes, A. P., On-Line Frequency Domain Information for Control of a Flexible-Link Robot with Varying Payload. *IEEE Transactions on Automatic Control*, 1989, **34**(12), pp. 1300-1304.

[23] Yurkovich, S., Pacheco, F. E., On Controller Tuning for a Flexible-Link Manipulator with Varying Payload. *Journal of Robotic Systems*, 1989, **6**(3), pp. 233-254.

Appendix A

Determination of System Constants

Note: with the exception of Table A.1 variables and symbols used in this Appendix are particular to each experiment and are not consistent with the rest of the thesis.

Experiment 1: Calculating the Motor Constant

Name Plate Data

TYPE: MT 30M4-35
Serial No: KA 6003
Small Electrical Motors Ltd. London
C-84-44-99
CONT. STALL TORQUE: 26 INLB
MAX RPM: 4000
Pulse Amps: 52 Volts: 140
INSUL: F
TACHO: 9.5V/1000RPM

The objective of this experiment is to calculate the motor constant $k\phi$. This was done by measuring Va, Ia, Ra, and the motor speed, ω. Then using the following equations, $k\phi$ can be calculated. Ra was measured at several different rotor positions and an average value was taken.

Ra = 1.23 ohms

$$V_a = E_a + I_a R_a$$
$$E_a = k\phi\omega$$

Experimental Results:

Va (V)	Ia (mA)	Tacho (V)	ω (RPM)	E (V)	Tacho (rad/s)	ω (rad/s)	$k\phi$ (Vs/rad)
5.431	384.2	1.343	93.7	4.912	14.80	14.71	0.3339
6.464	397.5	1.630	113.8	5.927	17.97	17.87	0.3317
7.499	411.4	1.917	133.5	6.944	21.13	20.97	0.3311
8.488	424.8	2.189	152.5	7.915	24.12	23.95	0.3305
9.492	429.0	2.461	171.2	8.913	27.12	26.89	0.3315
10.498	443.4	2.743	190.8	9.899	30.23	29.97	0.3303
11.503	453.2	3.023	210.3	10.891	33.23	33.03	0.3297
12.489	466.8	3.298	229.3	11.859	36.35	36.01	0.3293

$k\phi$ has been found to be approximately 0.33 Vs/rad. This is very close to the value that can be calculated by dividing the Nameplate Data voltage reading by MAX. RPM.

$$\frac{140V}{4000RPM * 2\pi/60} = 0.3342Vs/rad .$$

The tacho reading in the above table comes from the motor's tachometer. In column 6 it is shown as a value in rad/s, converted using the nameplate data conversion factor of 9.5 V/1000 RPM. The ω reading in the above table has been measured at the arm shaft. It is necessary to correct for the gear ratio before converting this value to rad/s, since it is the motor speed not the arm speed that we desire to measure. The gear ratio is 1.5 as determined from the number of teeth on the two gears. Therefore the motor turns 1.5 times as fast as the arm.

Experiment 2: Determining the Viscous and Coulomb Friction in the Motor and Shaft (without position potentiometer)

The purpose of this experiment is to plot $\frac{P}{\omega} = b\omega + T_f$. As this plot is a straight line, the numerical values of b and Tf can easily be determined. P is the electrical power to the motor at the armature, which ideally is converted to mechanical power.

$$P = E_a I_a$$
$$E_a = V_a - I_a R_a$$

Ra = 1.23 ohms

Ra was measured at several different rotor positions and an average value taken.
The ω referred to in the above equation is the motor speed in (rad/s).

Va(V)	Ia(mA)	Vtacho(V)	Ea (V)	P (W)	ω (rad/s)	P/ω
5.016	375	1.208	4.555	1.708	13.3122	0.1283
6.000	385	1.493	5.526	2.128	16.4529	0.1293
7.009	415	1.767	6.499	2.697	19.4723	0.1385
8.028	424	2.055	7.506	3.183	22.6461	0.1406
8.997	433	2.323	8.464	3.665	25.5995	0.1432
10.000	442	2.601	9.456	4.180	28.6630	0.1458
10.99	453	2.887	10.433	4.726	31.8147	0.1485
12.077	464	3.181	11.506	5.339	35.0546	0.1523
12.995	477	3.440	12.408	5.919	37.9088	0.1561
13.011	479	3.445	12.422	5.950	37.9639	0.1567
13.997	483	3.725	13.403	6.474	41.0495	0.1577
15.008	492	4.012	14.403	7.086	44.2122	0.1603

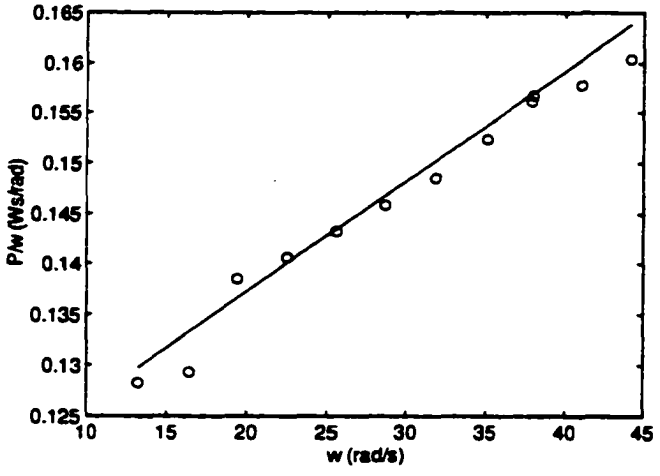

A plot of P/ω vs. ω is shown at left. A straight line is fitted to this data, in a least squares sense, and yields the equation:

$$\frac{P}{\omega} = 0.0011\omega + 0.1152$$

From this equation, numerical values for b and Tf are therefore 0.0011 Nms and 0.1152 Nm respectively.

Experiment 3: Determining Motor Inertia Based on Run-down Curve Data

This experiment seeks to determine the values for J, and T_f from the speed run-down curve of the motor.

This experiment was performed three times, corresponding to three different initial speeds. A voltage was applied to the armature to get the motor running at some initial speed. The voltage supply is then turned off and the resulting speed curve recorded.

Initial starting speeds for the motor were: 55.87 rad/s , 48.30 rad/s and 40.82 rad/s. The resulting run-down curves are shown below.

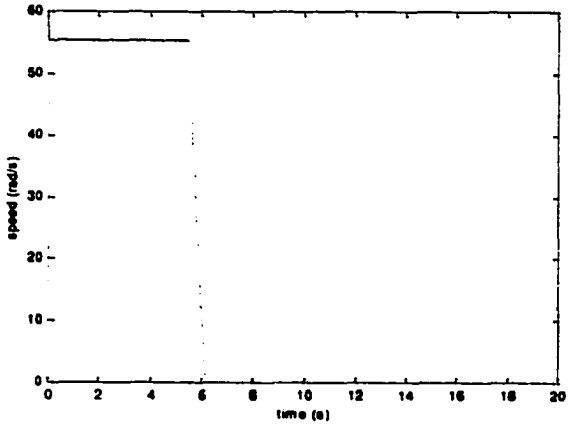

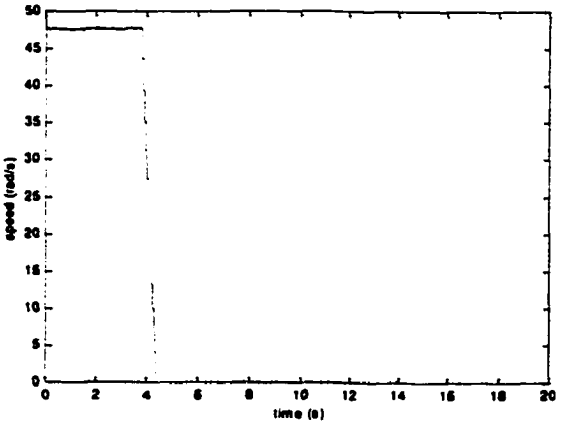

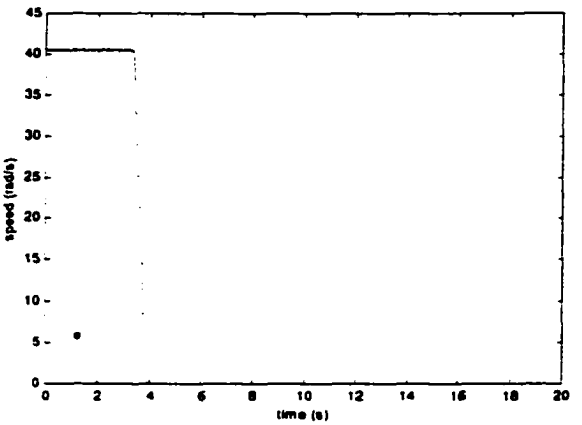

The equation for the speed of the motor based on the system constants with no external torque applied is [13]:

$$\omega(t) = \frac{-T_f}{b} + \left(\omega_o + \frac{T_f}{b}\right) e^{-\left(\frac{b}{J}\right)t} \qquad (1)$$

If b is assumed to be 0.0011 as previously determined experimentally, we can calculate J and T_f using the initial slope of the curve and the time it takes for the speed to drop to zero.

The initial slope of the run-down curve is $-\omega_o\left(\frac{b}{J}\right)$. By measuring this slope and knowing ω_o and b, J can, theoretically, be determined. To determine T_f, the time it takes for the curve to reach 0 rad/s, tc, is determined from the graph. Then with $\omega = 0$, b and J known, and tc as determined, T_f can be calculated from Equation (1). The data for the three experiments is shown in the table below.

ωo (rad/s)	b (Nms)	J (kgm^2)	tc (s)	T_f (Nm)	slope(rad/s^2) graph of speed
55.87	0.0011	0.0006365	0.714	0.02524	-96.55
48.30	0.0011	0.0005776	0.625	0.02322	-91.97
40.82	0.0011	0.0005212	0.575	0.01898	-86.15

However the value for J seems too small based on the physical size of this motor. The slope data is somewhat noisy however, so in practice this method is not very good.

If both T_f and b are assumed to be the values found in the power balance experiment, and only J is solved for, from Equation (1) the following values are obtained.

ωo (rad/s)	b (Nms)	J (kgm^2)	tc (s)	T_f (Nm)
55.87	0.0011	0.001770	0.714	0.11
48.30	0.0011	0.001745	0.625	0.11
40.82	0.0011	0.001848	0.575	0.11

These values seem more realistic. For comparison purposes, another method that can be used to find b, J and Tf, is to find the best values for these variables that fit our equation to the rundown curve (from the moment the power is switched off to when the motor stops). This was done using the fmins function in Matlab (based on the Nelder Mead technique [15]). The results are shown in the table below. Tf was assumed to be 0.1192 Nm.

b (Nms)	J (kgm^2)	Tf (Nm)	ωo (rad/s)
0.00156	0.002032	0.1192	55.87
0.00136	0.00194	0.1192	48.30
0.0017	0.002	0.1192	40.82

These values are more consistent with the table above and seem more reliable that just using the initial slope since they use the whole curve.

Experiment 4: Determining the Viscous and Coulomb Friction of the System Including the Flexible Arm.

When the arm is attached to the system, the hub cannot do a full rotation due to physical constraints of the setup. Therefore, a constant speed cannot be maintained and the previous power experiments cannot be repeated for this case. However, if the speed waveform is periodic in nature then a similar experiment can be performed.

If ω, is periodic and we integrate both sides of the equation:

$$\tau\omega = J\omega\dot{\omega} + b\omega^2 + T_f\omega$$

With respect to time, over one period, we get:

$$\int_{-T/2}^{T/2} \tau\omega dt = J\int_{\omega}^{\omega} \omega d\omega + \int_{-T/2}^{T/2} b\omega^2 dt + \int_{-T/2}^{T/2} T_f\omega dt$$

and $J\int_{\omega}^{\omega} \omega d\omega = 0$ therefore

$$\int_{-T/2}^{T/2} P dt = \int_{-T/2}^{T/2} b\omega^2 dt + \int_{-T/2}^{T/2} T_f\omega dt$$

and

$$\frac{\int_{-T/2}^{T/2} P\,dt}{\int_{-T/2}^{T/2} \omega^2\,dt} = b + \frac{\int_{-T/2}^{T/2} T_f \omega\,dt}{\int_{-T/2}^{T/2} \omega^2\,dt}$$

which is a straight line with intercept b and slope T_f.

$$P = E_a I_a$$
$$E_a = V_a - I_a R_a$$

Calculations for the straight-line equation were done for several different data sets, and values of T_f and b were found in each case. These values were then averaged to give T_f = 0.188 and b=0.0452, which are the total Coulomb and viscous friction respectively.

Experiment 5: Determination of Static Friction

The static friction was determined both for the motor and shaft, and for the complete system.

In each case the current to the motor was increased slowly until the speed of the motor was no longer zero. At this point the current was recorded. By multiplying this current by the motor constant the static friction torque is obtained. This experiment was repeated several times and the results averaged. For the motor and shaft only the static friction torque was 0.09487 Nm, for the combined system it was 0.2387 Nm.

Calculation of System Constants

From Experiment 2, the Coulomb friction for the motor and shaft was taken as 0.11 Nm, the viscous friction was 0.0011 Nms. To isolate the motor friction from the shaft friction it was assumed that the shaft friction and motor friction were equal. Therefore,

$$T_{fcoul} = T_{fcoulmotor} + \frac{1}{N} T_{fcoulshaft}$$

where N is the gear ratio. With T_{fcoul} = 0.11 Nm then, $T_{fcoulmotor}$ = 0.066 Nm. For the viscous friction

$$b = b_{motor} + \frac{1}{N^2} b_{shaft}$$

With b=0.0011 Nms then b_{motor} = 0.0008 Nms.

From Experiment 4, the viscous and Coulomb friction for the combined system was taken to be b = 0.0452 Nms and T_f = 0.188 Nm. Knowing the friction values for the motor alone, we can solve for the friction values for the arm.

$$T_f = T_{fcoulmotor} + \frac{1}{N} T_{fcoularm}$$

Therefore, $T_{fcoularm}$ = 0.183 Nm

$$b = b_{motor} + \frac{1}{N^2} b_{arm}$$

Therefore, b_{arm} = 0.1 Nms

From Experiment 3 the motor inertia was taken as J_m = 0.00193 kgm^2. The arm inertia was calculated from the arm dimensions and mass and without payload is 0.15804 kgm^2.

With the static friction of the motor equal to 0.09487 Nm and the total static friction of the system equal to 0.2387 Nm as determined in experiment 5, the static friction of the arm is 0.2157 Nm as determined from

$$T_{fstatictotal} = T_{fstaticmotor} + \frac{1}{N} T_{fstaticarm}$$

Thus the values used in the simulations are:

System Constant Values used in Simulation	
J_m = 0.00193 kgm^2 T_{mf} - 0.066 Nm (Coulomb) - 0.09487 Nm (static) T_{af} - 0.183 Nm (Coulomb) - 0.21574 Nm (static) J_a = 0.158 + $m_3 d_3^2$ kgm^2	r_1 / r_2 = 1/N = 1/1.5 b_m = 0.0008 Nms b_s = 0.1 Nms m_3 = Payload Mass (kg) d_3 = 1 m $\Delta\theta$ = 0.01164

Table A.1 System Constant Values used in Simulations